

Large-scale magnetic topologies of late M dwarfs^{*}

J. Morin^{1,*†}, J.-F. Donati¹, P. Petit¹, X. Delfosse², T. Forveille², M.M. Jardine³

¹ *LATT, Université de Toulouse, CNRS, 14 Av. E. Belin, F-31400 Toulouse, France*

^{*} *Now at: Dublin Institute for Advanced Studies, School of Cosmic Physics, 31 Fitzwilliam Place, Dublin 2, Ireland*

² *Université. J. Fourier (Grenoble 1)/CNRS; Laboratoire d'Astrophysique de Grenoble (LAOG, UMR 5571); F-38041 Grenoble, France*

³ *School of Physics and Astronomy, Univ. of St Andrews, St Andrews, Scotland KY16 9SS, UK*

22 May 2018, Revision:2.02

ABSTRACT

We present here the final results of the first spectropolarimetric survey of a small sample of active M dwarfs, aimed at providing observational constraints on dynamo action on both sides of the full-convection threshold (spectral type M4). Our two previous studies (Donati et al. 2008b; Morin et al. 2008b) were focused on early and mid M dwarfs. The present paper examines 11 fully convective late M dwarfs (spectral types M5–M8). Tomographic imaging techniques were applied to time-series of circularly polarised profiles of 6 stars, in order to infer their large-scale magnetic topologies. For 3 other stars we could not produce such magnetic maps, because of low variability of the Stokes V signatures, but were able to derive some properties of the magnetic fields.

We find 2 distinct categories of magnetic topologies: on the one hand strong axisymmetric dipolar fields (similar to mid M dwarfs), and on the other hand weak fields generally featuring a significant non-axisymmetric component, and sometimes a significant toroidal one. Comparison with unsigned magnetic fluxes demonstrates that the second category of magnetic fields shows less organization (less energy in the large scales), similarly to partly convective early M dwarfs. Stars in both categories have similar stellar parameters, our data do not evidence a separation between these 2 categories in the mass-rotation plane.

We also report marginal detection of a large-scale magnetic field on the M8 star VB 10 featuring a significant toroidal axisymmetric component, whereas no field is detectable on VB 8 (M7).

Key words: stars: magnetic fields – stars: low-mass – stars: rotation – techniques: spectropolarimetry

1 INTRODUCTION

Magnetic field is a key parameter in theories of stellar formation and evolution. In cool stars, it powers several activity phenomena, observed on a wide range of wavelengths and timescales, which provide a rough proxy of the averaged field strength. The well-established rotation-activity relation (e.g., Noyes et al. 1984) supports the idea of a dynamo-generated magnetic field in these stars.

Larmor (1919) first proposed that the solar magnetic field could be induced by plasma motions, already pointing out the importance of shear (Ω effect) to generate strong toroidal fields and thus explain Hale's polarity law of sunspots. Parker (1955) completed the basic picture of the solar dynamo by introducing the α effect (convection made cyclonic by the Coriolis force) to address the issues of Cowling's anti-dynamo theorem (Cowling 1933) and the regeneration of a poloidal field component from a toroidal one. The $\alpha\Omega$ dynamo has thereafter been thoroughly debated and improved (e.g. Babcock 1961; Leighton 1969). More recently, helioseismology has been able to probe the solar interior and revealed the existence of a thin layer of strong shear located at the base of the convection zone: the tachocline (e.g., Spiegel & Zahn 1992). Although many aspects of the solar magnetism are still not thoroughly understood, recent theoretical and numerical studies have pointed

^{*} Based on observations obtained at the Canada-France-Hawaii Telescope (CFHT). CFHT is operated by the National Research Council of Canada, the Institut National des Science de l'Univers of the Centre National de la Recherche Scientifique of France (INSU/CNRS), and the University of Hawaii.

[†] E-mail: jmorin@cp.dias.ie

out the crucial role of the tachocline as the place of storage and amplification of strong toroidal fields (e.g., [Ossendrijver 2003](#); [Charbonneau 2005](#)).

New insight on dynamo processes can be gained from the exploration of magnetic fields of cool stars, probing the dynamo response in very non-solar regimes of parameters (e.g., fast rotation, deeper or shallower convection zone). M dwarfs are particularly interesting since those below $\sim 0.35 M_{\odot}$ (e.g., [Chabrier & Baraffe 1997](#)) are fully convective and therefore do not possess a tachocline and presumably cannot host a solar-type dynamo. Yet, many M dwarfs are known to be active, and these stars follow the usual rotation-activity relation (e.g., [Delfosse et al. 1998](#); [Reiners & Basri 2007](#); [Kiraga & Stepien 2007](#); [West et al. 2004](#)). However the strong correlation between X-ray and radio luminosities established by [Guedel & Benz \(1993\)](#) for stars of spectral types ranging from F to mid M, is no longer valid for very low mass dwarfs which exhibit very strong radio emission whereas X-ray emissions dramatically drop ([Berger 2006](#)). Magnetic fields were also directly detected at photospheric level through Zeeman effect both in unpolarised (e.g., [Saar & Linsky 1985](#); [Johns-Krull & Valenti 1996](#); [Reiners & Basri 2006](#)) and circularly polarised ([Donati et al. 2006a](#)) line profiles.

Spectropolarimetry combined with tomographic imaging techniques is the optimal technique to investigate the magnetic topologies of M dwarfs (see [Sec. 3](#) for more details). By recovering the large-scale component of stellar magnetic fields, we can provide dynamo theorists with observables directly comparable with their modeling (axisymmetry, relative importance of the poloidal and toroidal components, characteristic scales...). Previous results have already produced strong constraints: [Donati et al. \(2006a\)](#) and [Morin et al. \(2008a\)](#) (hereafter M08a) demonstrated that the fully convective fast rotator V374 Peg is able to trigger a strong large-scale axisymmetric poloidal field steady on a timescale of 1 year; and exhibits a very low level of differential rotation ($\sim \frac{d\Omega_{\odot}}{10}$). From the analysis of a sample of early and mid M dwarfs [Donati et al. \(2008b\)](#) and [Morin et al. \(2008b\)](#) (hereafter D08 and M08b respectively) observed a strong change near the theoretical full-convection threshold: while partly convective stars possess a weak non-axisymmetric field with a significant toroidal component, fully convective ones exhibit strong poloidal axisymmetric dipole-like topologies. Differential rotation also drops by an order of magnitude across the boundary, the observed fully convective stars exhibit nearly solid body rotation. D08 and M08b also report a sharp transition in the rotation-large-scale magnetic field relation close to the full-convection boundary, whereas no such gap is visible in the rotation-X-ray relation. Considering that X-ray emission is a good proxy for the total magnetic energy, it suggests that a sharp transition in the characteristic scales of the magnetic field occurs near the full-convection limit. This point was further confirmed for a few stars by [Reiners & Basri \(2009\)](#) who report that the ratio of the magnetic fluxes measured from circularly-polarised and unpolarised lines dramatically changes across the fully convective limit. Several theoretical studies have addressed the challenging issue of dynamo action in fully convective stellar interiors. [Durney et al. \(1993\)](#) first proposed that without a tachocline of shear, convec-

tion and turbulence should play the main role at the expense of differential rotation, generating a small-scale field. [Küker & Rüdiger \(1999\)](#) and [Chabrier & Küker \(2006\)](#) performed mean-field modeling of dynamo action in fully convective stars and found purely non-axisymmetric α^2 solutions, indicating that these objects can sustain large-scale magnetic fields. Subsequent direct numerical simulations by [Dobler et al. \(2006\)](#) and [Browning \(2008\)](#) both realized large-scale dynamo action with a significant axisymmetric component of the resulting magnetic field. The latter also achieved magnetic energy in equipartition with kinetic energy and therefore Maxwell stresses strong enough to quench differential rotation, resulting in nearly solid-body rotation. Despite these recent advances, the precise causes of differences between dynamo in fully and partly convective stars are not completely understood, and theoretical studies need observational guidance.

In the present paper, we extend our spectropolarimetric study to 11 late M dwarfs (spectral types ranging from M5 to M8). After a brief presentation of the stellar sample and of spectropolarimetric observations, we describe the main principles of the tomographic imaging process. The Zeeman-Doppler Imaging (ZDI hereafter) analysis is then detailed for 6 stars. For 3 other late M dwarfs, it is not possible to derive a definitive magnetic map because of the very low level of variability in the Stokes V signatures, but we can still infer some information about their magnetic topologies. For the very faint stars VB 8 and VB 10, the noise level is too high to allow definite detection of the circularly polarised signatures in individual LSD spectra. By averaging the spectra of each data set, we marginally detect a large-scale magnetic field on VB 10, and show a tentative ZDI reconstruction. We finally discuss these results and conclude on the implications of our study for the understanding of dynamo processes in fully convective stars.

2 OBSERVATIONS

2.1 Presentation of the sample

For this first spectropolarimetric survey, we selected 23 active main-sequence M dwarfs, mostly from the rotation-activity study by [Delfosse et al. \(1998\)](#), covering a wide range of masses and rotation periods (although for a given mass the extent in rotation period is rather restricted). In the present paper we focus on the low-mass end of the sample (0.08–0.20 M_{\odot}): GJ 51, WX UMa, DX Cnc, GJ 1245 B, GJ 1156 and GJ 3622 are thoroughly studied with tomographic imaging techniques. We also present a brief study of the large-scale magnetic topologies of GJ 1224, GJ 1154 A, CN Leo, VB 8 and VB 10 ([section 10](#)).

All these stars are known to show signs of activity in $H\alpha$ or X-rays (e.g. [Gizis et al. 2002](#); [Schmitt & Liefke 2004](#)), and photospheric magnetic fields have been measured on most of them from the analysis of Zeeman broadening in molecular bands (see below). The main properties of the sample, inferred from this work or collected from previous ones, are shown in [Tab. 1](#).

Stellar masses are computed from the mass-luminosity relation derived by [Delfosse et al. \(2000\)](#), based on J band absolute magnitude inferred from apparent magnitude mea-

Table 1. Fundamental parameters of the stellar sample. Spectral types are taken from Reid et al. (1995). Formal error bars derived from our study are mentioned between brackets for M_* , $R \sin i$, R_* (1σ) and P_{rot} (3σ), they apply to the last digit of the preceding number. See Sec. 2.1 for more details and a discussion about uncertainties.

Name	ST	M_* (M_\odot)	$v \sin i$ (km s^{-1})	Bf (kG)	P_{rot} (d)	τ_c (d)	Ro (10^{-2})	$R \sin i$ (R_\odot)	R_* (R_\odot)	i ($^\circ$)
GJ 51	M5	0.21 (3)	12	–	1.02 (1)	83	1.2	0.24 (2)	0.22 (3)	60
GJ 1156	M5	0.14 (1)	17 ^b	2.1 ^b	0.491 (2)	94	0.5	0.16 (< 1)	0.16 (1)	60
GJ 1245 B	M5.5	0.12 (< 1)	7 ^a	1.7 ^a	0.71 (1)	97	0.7	0.10 (2)	0.14 (< 1)	40
WX UMa	M6	0.10 (< 1)	5 ^b	> 3.9 ^b	0.78 (2)	100	0.8	0.07 (1)	0.12 (< 1)	40
DX Cnc	M6	0.10 (1)	13 ^a	1.7 ^a	0.46 (1)	100	0.5	0.07 (1)	0.11 (< 1)	60
GJ 3622	M6.5	0.09 (< 1)	3 ^c	–	1.5(2)	101	1.5	0.09 (6)	0.11 (< 1)	60
GJ 1154 A	M5	0.18 (1)	6 ^b	2.1 ^b	≤ 1.7	88	≤ 1.9	–	0.20 (1)	–
GJ 1224	M4.5	0.15 (1)	$\leq 3^a$	2.7 ^a	≤ 4.3	93	≤ 4.6	–	0.17 (1)	–
CN Leo	M5.5	0.10 (< 1)	3 ^a	2.4 ^a	≤ 2.0	99	≤ 2.0	–	0.12 (< 1)	–
VB 8	M7	0.09 (< 1)	5 ^a	2.3 ^a	≤ 1.0	101	≤ 1.0	–	0.10 (< 1)	–
VB 10	M8	0.08 (< 1)	6 ^a	1.3 ^a	≤ 0.8	102	≤ 0.8	–	0.09 (< 1)	–

^a Reiners & Basri (2007)

^b Reiners et al. (2009)

^c Mohanty & Basri (2003)

measurements of 2MASS (Cutri et al. 2003) and *Hipparcos* parallaxes (ESA 1997). Formal error bars, as derived from uncertainties on these measurements are mentioned. The intrinsic dispersion of the relation is estimated to be lower than 10 %. Radius and bolometric luminosity suited to the stellar mass are computed from NextGen models (Baraffe et al. 1998), formal error-bars on stellar mass are propagated. The accuracy of these models for active M dwarfs is a debated subject (e.g., Ribas 2006), but recent studies indicate that the agreement with observations is very good for late M dwarfs (Demory et al. 2009). For all stars except GJ 51, projected rotational velocities ($v \sin i$) are available from previous spectroscopic studies. The uncertainties on $v \sin i$ are typically equal to 1 km s^{-1} . For each star, we also mention the rotation period (P_{rot}) derived from our analysis (see Sec. 3.3), and $R \sin i$ is straightforwardly deduced (with propagated error bar). An estimate of the inclination angle of the rotation axis on the line-of-sight (i) is obtained by comparing $R \sin i$ and the theoretical radius. With this estimate the typical error is of the order of 10° for low and moderate inclinations, and 20° for high inclination angles, this is precise enough for the imaging process. The effect of these uncertainties on the reconstructed magnetic maps is discussed in Sec. 3.4.

We also mention unsigned magnetic fluxes from the literature (whenever available in Reiners & Basri 2007 and Reiners et al. 2009) empirically derived from unpolarised molecular (FeH) line profiles. These estimates result from the comparison with reference spectra of an active and an inactive star (corrected for spectral type and rotational broadening) which are used to calibrate the relation between broadening of magnetically sensitive lines and magnetic flux (Reiners & Basri 2006). The authors estimate that the precision of the method lies in the 0.5–1 kG range. As this method is not sensitive to the vector properties of the magnetic field, the Bf values reflect the overall magnetic flux on the surface of the star. Since Stokes V signatures corresponding to neighbouring zones of fields with opposite polarities cancel each other, our spectropolarimetric measurements are not

sensitive to tangled fields and only recover the uncanceled magnetic flux corresponding to the large-scale component of the magnetic topology. Therefore the ratio of both magnetic fluxes is a clear indication of the degree of organization of the observed magnetic field.

The convective Rossby number (Ro), which is the ratio of the rotation period and the convective turnover time, is believed to be the relevant parameter to study the impact of rotation on dynamo action in cool stars (Noyes et al. 1984). In Table 1, we mention Rossby numbers based on empirical convective turnover times derived by Kiraga & Stepien (2007) from the rotation–activity relation in X-rays. These turnover times are *ad-hoc* fitting parameters that reflect more the relation between activity and rotation at a given mass than an actual turnover time at a specific depth in the convection zone. However, the resulting Rossby numbers allow us to compare the effect of rotation on magnetic field generation in stars having different masses.

2.2 Instrumental setup and data reduction

Observations presented here were collected between June 2006 and July 2009 with the ESPaDOnS spectropolarimeter at CFHT. ESPaDOnS provides full coverage of the optical domain (370 to 1,000 nm) in a single exposure, at a resolving power of 65,000, with a peak efficiency of 15% (telescope and detector included).

Data Reduction is carried out with LIBRE-ESPRIT, a fully-automated dedicated pipeline provided to ESPaDOnS and NARVAL users, that performs optimal extraction of the spectra following the procedure described in Donati et al. (1997) that is based on Horne (1986) and Marsh (1989). Each set of 4 individual sub-exposures taken in different polarimetric configuration are combined together to produce Stokes I (unpolarised intensity) and V (circularly polarised) spectra, so that all spurious polarisation signatures are cancelled to first order (Semel et al. 1993; Donati et al. 1997). In addition, all spectra are automatically corrected

for spectral shifts resulting from instrumental effects (e.g., mechanical flexures, temperature or pressure variations) using telluric lines as a reference. Though not perfect, this procedure allows spectra to be secured with a radial velocity (RV) internal precision of better than 0.030 km s^{-1} (e.g., [Moutou et al. 2007](#)).

The peak signal-to-noise ratios (S/N) per 2.6 km s^{-1} velocity bin range from 51 to 245, mostly depending on the magnitude of the target and the weather conditions. An overview of the observations is presented in Table 2, the full journal of observations is available in the electronic version. Using the Least-squares deconvolution technique (LSD, [Donati et al. 1997](#)), polarimetric information is extracted from most photospheric atomic lines and gathered into a single synthetic profile of central wavelength $\lambda_0 = 750 \text{ nm}$ (800 nm for VB 8 and 10). The corresponding effective Landé factor g_{eff} (computed as a weighted average on available lines) is close to 1.2 for all the stars of our sample. The line list for LSD was computed from an Atlas9 local thermodynamic equilibrium model ([Kurucz 1993](#)) matching the properties of our whole sample, and contains about 5,000 moderate to strong atomic lines. We notice a multiplex gain of about 10 (5 for VB 8 and 10) with respect to the peak S/N of the individual spectra of our sample. Although all the stars in the sample are active, some exhibit Stokes V LSD signatures just above noise level (e.g. DX Cnc), whereas on others we detect very strong signatures, with peak-to-peak amplitudes as high as 1.8% of the unpolarised continuum level (for WX UMa). Temporal variations, due to rotational modulation, of the Zeeman signatures is obvious for some stars, whereas it is very weak on others, depending e.g., on the inclination angle of their rotation axis with respect to the line of sight, the complexity and the degree of axisymmetry of their magnetic topology.

For each observation we compute the corresponding longitudinal magnetic field (i.e. the line of sight projection) from the Stokes I and V LSD profiles through the relation:

$$B_l(\text{G}) = -2.14 \times 10^{11} \frac{\int v V(v) dv}{\lambda_0 g_{\text{eff}} c \int [I_c - I(v)] dv}, \quad (1)$$

([Rees & Semel 1979](#); [Donati et al. 1997](#); [Wade et al. 2000](#)) where v is the radial velocity in the star's rest frame, λ_0 , in nm, is the mean wavelength of the LSD profile, c is the velocity of light in vacuum in the same unit as v , g_{eff} is the value of the mean Landé factor of the LSD line, and I_c the continuum level.

In the rest of the paper, all data are phased according to the following ephemeris:

$$\text{HJD} = \text{HJD}_0 + P_{\text{rot}} E, \quad (2)$$

where $\text{HJD}_0 = 2453850$ for WX UMa, and $\text{HJD}_0 = 2453950$ for the other stars; and P_{rot} is the rotational period used as an input for ZDI and given in Table 1.

3 DATA MODELLING

Zeeman Doppler imaging ([Donati & Brown 1997](#)) aims at assessing stellar magnetic topologies (at photospheric level), from the analysis of time-series of high spectral resolution

spectropolarimetric observations. In this part we briefly remind the reader with the main properties of this technique and details of our implementation. A more complete description can be found in M08b and references therein.

ZDI is an inverse problem, the associated direct problem consists in computing the Stokes I and V spectra for a given magnetic map. The stellar surface being sampled on a grid of $\sim 1,000$ cells, the local Stokes I and V profiles are computed from a model based on Unno-Rachkovsky's equations, for a given magnetic map. The magnetic field is decomposed into its poloidal and toroidal components and described as a set of spherical harmonics-like coefficients, as implemented by [Donati et al. \(2006b\)](#). We introduce two filling factors that account for subgrid cancellation of polarised signatures corresponding to fields of opposite polarities, and allows us to accurately reproduce the LSD line profiles (M08b). The stellar spectrum is then obtained by a disk integration taking into account Doppler shift and limb-darkening.

3.1 Rotational modulation of polarised lines

In the presence of a magnetic field one can observe the Zeeman effect on spectral lines: (i) unpolarised lines (Stokes I) are broadened with respect to the null field configuration and (ii) polarised signatures (Stokes Q , U and V) show up. Here we only study circular polarisation (Stokes V), which is sensitive to the strength and polarity of the line-of-sight projection of the field. Because of the combination of stellar rotation and Doppler effect:

- The contribution of a photospheric region to the stellar spectrum is correlated with its longitude (at first order). Thus, as a magnetic region crosses the stellar disk under the effect of rotation, the corresponding polarised signal migrates from the blue to the red wing of the line.
- The amplitude of this migration depends on the spot's latitude (no migration for a polar spot, maximum migration from $-v \sin i$ to $+v \sin i$ for an equatorial one).
- The evolution of the signature during this migration (as the angle between the field vector and the line of sight changes with rotation) is characteristic of the field orientation (e.g. signature of constant polarity for radial field, and polarity reversal for azimuthal field).

Therefore, from a series of polarised spectra providing even and dense sampling of stellar rotation, it is possible to reconstruct a map for the photospheric magnetic field.

3.2 Magnetic field reconstruction: inverse problem

Starting from a null-field configuration, the series of spectra computed from a test field is iteratively compared to the observed one, until a given χ_r^2 level is reached. As the problem is partly ill-posed (several magnetic configurations can match a data set equally well), the maximum entropy solution is selected. The spatial resolution of ZDI depends on $v \sin i$ as a rule of thumb. The highest degree available in the field reconstruction is:

$$\ell_{\text{max}} \simeq \max\left(\frac{2\pi v \sin i}{W}; \ell_{\text{min}}\right) \quad (3)$$

Table 2. Synthetic journal of observations. Observation year and number of spectra collected are given in columns 2 and 3. Columns 4 and 5 respectively list the peak signal to noise ratio (per 2.6 km s^{-1} velocity bin) and the rms noise level (relative to the unpolarised continuum level and per 1.8 km s^{-1} velocity bin) in the average circular polarisation profile produced by Least-Squares Deconvolution (see text) — we precise minimum and maximum values obtained for each observing run. The average value and standard deviation of the longitudinal magnetic field (see Eq. 1) and the radial velocity measurements are given in columns 6 and 7. The rotation cycle bounds of column 8 are computed with the rotation periods mentioned in Table 1. Complete observation logs are available in the electronic version of the article.

Name	Year	n_{obs}	S/N	σ_{LSD} ($10^{-4} I_c$)	B_ℓ (G)	RV (km s^{-1})	Cycle
GJ 51	2006	6	128–165	7.7–10.1	-990 (313)	-5.52 (0.20)	5.0–9.9
–	2007	9	159–198	5.7–7.0	-1657 (280)	-6.36 (0.74)	412.7–418.7
–	2008	9	118–181	6.9–10.3	-1219 (407)	-6.60 (0.57)	788.0–794.1
GJ 1156	2007	6	120–181	6.8–11.0	82 (72)	5.96 (0.24)	431.9–442.0
–	2008	5	127–158	10.4–8.4	-47 (166)	5.81 (0.13)	1091.6–1095.9
–	2009	9	183–195	6.5–6.9	24 (111)	5.73 (0.24)	1812.7–1817.0
GJ 1245 B	2006	6	158–191	7.1–8.8	-52 (163)	5.42(0.11)	4.2–14.0
–	2007	6	182–226	5.7–7.4	-17 (128)	5.38 (0.10)	597.0–601.2
–	2008	10	138–194	7.2–10.1	-6 (67)	5.46 (0.09)	1054.6–1057.8
WX UMa	2006	8	67–142	19.8–9.6	-1506 (453)	70.25 (0.53)	0.5–4.4
–	2007	6	115–154	8.4–11.8	-1757 (405)	69.95 (0.06)	341.8–349.5
–	2008	4	63–129	10.4–21.4	-1811 (271)	70.15 (0.24)	755.8–758.6
–	2009	11	113–163	8.0–12.5	-1496 (271)	69.83 (0.21)	1214.9–1218.9
DX Cnc	2007	5	119–179	8.3–12.3	132 (76)	10.55 (0.07)	460.7–471.5
–	2008	7	90–161	9.4–16.7	92 (52)	10.44 (0.56)	1160.6–1169.5
–	2009	9	106–187	7.8–14.8	67 (44)	10.67 (0.10)	2012.8–2019.6
GJ 3622	2008	8	128–167	8.9–11.1	-32 (29)	2.27 (0.28)	397.2–402.6
–	2009	6	101–162	9.3–15.0	-26 (26)	2.37 (0.05)	617.3–620.0
GJ 1154 A	2007	6	118–167	7.0–10.5	-714 (76)	-12.83 (0.11)	–
–	2008	4	86–154	8.3–15.9	-700 (75)	-12.92 (0.18)	–
GJ 1224	2008	12	51–185	5.8–19.7	-563 (41)	-32.68 (0.04)	–
CN Leo	2008	4	172–245	4.5–6.7	-691 (54)	19.62 (0.05)	–
VB 8	2009	9	83–107	15.7–20.0	29 (53)	15.39 (0.11)	–
VB 10	2009	9	68–80	22.5–25.7	58 (61)	36.23 (0.14)	–

where W is the unpolarised local profile width ($\sim 9 \text{ km s}^{-1}$ for an inactive non-rotating M dwarf, M08a). The first term in the max function corresponds to the limit of high $v \sin i$, when line broadening is mostly due to rotation and the line profile can actually be seen as one 1-D map of the photospheric magnetic field. The second term, ℓ_{\min} is the minimum resolution available in the low $v \sin i$ limit, when Doppler shift is small and the information on the field topology mostly comes from the temporal evolution of the shape and amplitude of the polarised signatures. ℓ_{\min} can range from 4 to 8 mostly depending on the signal to noise ratio of the data (D08, M08b).

3.3 Period determination

Since ZDI is based on the analysis of rotational modulation, important inputs of the code are: the projected equatorial velocity ($v \sin i$), the inclination angle of the rotation axis with respect to the line of sight (i) and the rotation period (P_{rot}). As no previous definite period measurement exists for any star of our late M subsample, we use ZDI to provide a constraint on this parameter. For each star, given the $v \sin i$ and the theoretical radius (corresponding to the stellar mass) we can derive an estimate of the maximum value for the rotation period as :

$$P_{\text{max}} = 50.6145 \times \frac{R_\star}{v \sin i}, \quad (4)$$

where P_{max} is expressed in days, R_\star in unit of R_\odot and $v \sin i$ in km s^{-1} . We test period values in a reasonable range ($< 1.2 \times P_{\text{max}}$), and derive the most probable period as the one resulting in the minimum χ_r^2 at a given informational content (i.e. a given averaged magnetic flux value). We try to resolve aliases by comparing the multiple data sets available for each star. By fitting a parabola to the resulting χ_r^2 curve close to the minimum, we derive the optimal value of P_{rot} and the associated formal error bar (see M08b for more details). Since several data sets are available for each star, we mention the smallest 3σ error bar in Tab. 1. For all the studied stars periods inferred from different data sets are compatible with each other within the width of the associated error bars.

3.4 Uncertainties on the magnetic maps

Due to the use of a maximum entropy method, magnetic maps reconstructed with ZDI are optimal in the sense that any feature present in the map is actually required to fit the data. However this method does not allow us to derive formal error bars on the reconstructed maps.

Numerical experiments demonstrate that ZDI provides reliable maps and is robust with respect to reasonable un-

certainties on various parameters and data incompleteness (e.g., Donati & Brown 1997). In addition, our implementation based on spherical harmonics and poloidal/toroidal decomposition successfully reconstructs global topologies such as low-degree multipoles, as well as more complex configurations (e.g., Donati et al. 2006b). We also find that ZDI maps are robust with respect to the selected entropy weighting scheme, provided that phase coverage is complete enough.

We try to assess the effects of the uncertainties on the input parameters (see Sec. 2.1), on the derived magnetic quantities in a similar way as Petit et al. (2008). For each data set we perform several reconstructions with input parameters $v \sin i$, i , and P_{rot} varying over the width of the error bars and check the resulting map and its properties, thus providing a quantitative analysis of the robustness of our reconstructions to these uncertainties. We therefore obtain “variability bars” rather than formal error bars. Given the small uncertainties on the rotation period, varying this parameter within the 3σ error bar has negligible effect on the reconstructed maps. The magnetic quantities listed in Tab. 9 to characterize the repartition of magnetic energy into different components are affected in different ways by variations of the input parameters. In particular, the decomposition between poloidal and toroidal energy is very robust, the observed variation is less than 10 % of the reconstructed magnetic energy. The fraction of magnetic energy in axisymmetric modes varies by up to 20 % due to uncertainties on input parameters. The most important effect observed is a cross-talk between the dipole component and higher degree multipoles (in particular the quadrupole), the variation of the fraction of energy in the dipole is in the 10–30% range. The variability bars on the reconstructed magnetic flux are of the order of 30 %.

4 GJ 51

We have acquired a total of 24 spectra on GJ 51 split in 3 series collected on 3 successive years (see Tab. 2). All Stokes V spectra exhibit a strong signature of constant polarity (radial field directed toward the star). Temporal variation inside each data set is detectable and likely due to rotational modulation. It mainly consists of an evolution of the signature’s amplitude. To our knowledge, no previously published measurement of P_{rot} or $v \sin i$ exist for this star. From our LSD Stokes I profiles we measure mean RV values of -5.52 , -6.36 , and -6.60 km s^{-1} in 2006, 2007 and 2008, respectively. These values are in agreement with the previously published RV = -7.3 km s^{-1} (Gizis et al. 2002). Our RV measurements also reveal a drift between the 3 epochs, too large to be due to convection and that may indicate a companion orbiting around this star. We also observe strong RV temporal variations inside each data set presumably due to magnetic activity (see Tab. 2), well above the intrinsic precision of the instrument (see Sec. 2.2). Our analysis of both the unpolarised and polarised spectra leads us to $v \sin i = 12 \text{ km s}^{-1}$ and $P_{\text{rot}} = 1.02 \text{ d}$, this is close to the 1.06 d period derived from the MEarth¹ photometric data (J. Irwin, private communication). From these values

Table 3. Fit achieved for the 3 spectral time-series obtained on GJ 51. The imaging process is guided towards a mostly axisymmetric solution, see text. In columns 2 we give the maximum degree of spherical harmonics used for ZDI reconstruction. Columns 3–6 respectively list the initial χ_r^2 (i.e. without magnetic field), the χ_r^2 achieved with the imaging process, and the average and peak value of the magnetic flux on the reconstructed map.

Epoch	ℓ_{ZDI}	χ_{r0}^2	χ_{rf}^2	$\langle B \rangle$ (kG)	B_{max} (kG)
2006	5	6.17	1.00	1.61	3.86
2007	5	24.53	1.00	1.58	5.02
2008	5	15.20	1.00	1.65	4.68

we infer $R \sin i = 0.24 R_{\odot}$, whereas for $M_{\star} = 0.20 M_{\odot}$ evolutionary models expect $R_{\star} = 0.21 R_{\odot}$. We conclude that the inclination angle of the rotation axis with respect to the line-of-sight must be high, and set $i = 60^{\circ}$ for ZDI. We note that for $P_{\text{rot}} = 1.02 \text{ d}$ none of our data set provide a complete sampling of the stellar rotation, the best one being the 2008 data set which covers 30% of the rotation cycle. Despite this poor phase coverage, Stokes V profiles collected at the 3 epochs are similar, suggesting that the magnetic field is stable and mostly axisymmetric.

Setting $\ell_{\text{ZDI}} = 5$ for the magnetic field decomposition, it is possible to fit each of our 3 data sets with $\chi_r^2=1$. The resulting magnetic maps feature a strong non-axisymmetric component with a dipole tilted toward the observer, in particular those inferred from our 2006 and 2007 spectra. This is surprising, it is indeed very unlikely that we observe three times GJ 51 at the same phase (when the magnetic pole is crossing the line of sight).

The magnetic map reconstructed by ZDI is highly dependent on the precise form of the entropy, whereas it is generally not the case, indicating that this reconstruction is particularly ill-posed. We suggest this is due to the lack of information associated with the poor phase coverage, the reconstructed solution is strongly influenced by the maximum entropy constraint: the resulting map is therefore mainly composed of a spot of radial field facing the observer.

We perform another reconstruction of the magnetic field of GJ 51, with addition of *a priori* information in the process, so that it preferentially converges toward a mostly axisymmetric solution, as far as it allows to fit the data at the prescribed χ^2 level. This is done by putting a strong entropy penalty on non-axisymmetric modes, similarly to the method used by Donati et al. (2008a) to drive the reconstructed topology towards antisymmetry with respect to the center of the star. In these conditions, we can also fit our 3 data sets with $\chi_r^2=1$. The resulting magnetic maps for the 3 epochs are very similar (Fig. 2). The corresponding synthetic spectra are plotted along with the data on Fig. 1. We find similar results at all epochs: the magnetic topology is almost purely poloidal and axisymmetric, it is mainly composed of a very strong dipole aligned with the rotation axis (see tables 3 and 9 for more details). The azimuthal and meridional component of the field somehow differ between the three epochs, but we consider that this is not significant given the weak constraint provided by our data. These

¹ Irwin et al. (2009)

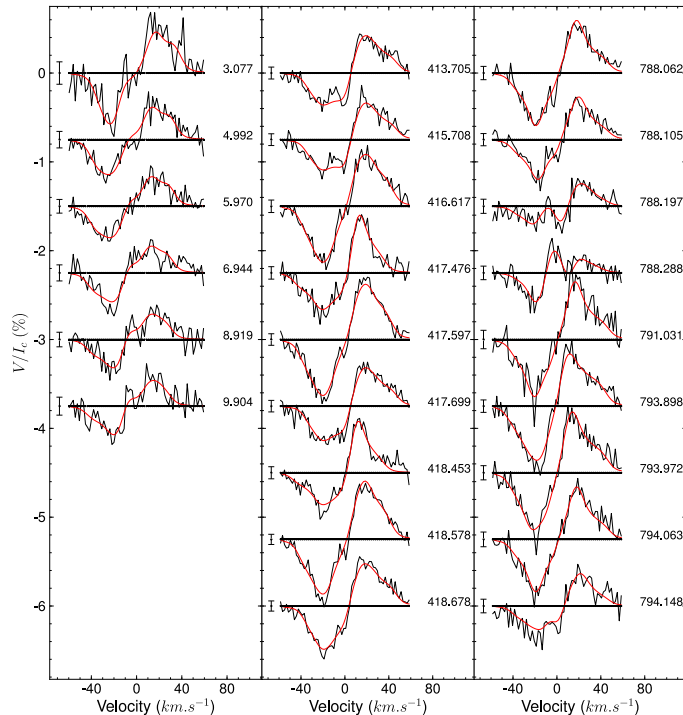


Figure 1. Time-series of Stokes V profiles of GJ 51, in the rest-frame of the star, from our 2006 (left-hand column), 2007 (middle column) and 2008 (right-hand column) data sets. Synthetic profiles corresponding to our magnetic models (red lines) are superimposed to the observed LSD profiles (black lines). Left to each profile a $\pm 1\sigma$ error bar is shown. The rotational phase and cycle of each observation is also mentioned right to each profile. Successive profiles are shifted vertically for clarity purposes and the associated reference levels ($V = 0$) are plotted as dotted lines.

maps are not the only solution permitted by our data, but we believe that they represent the most probable one.

Variability bars are of the same order of magnitude as for the other stars. The almost purely poloidal nature of the magnetic field is robust to uncertainties on the input parameters i and $v \sin i$. In addition, when varying these parameters, the topology always features a strong purely axisymmetric component (i.e. more than 45% of the magnetic energy is reconstructed in $m = 0$ modes) and the main reconstructed mode is the radial component of a dipole aligned with the rotation axis. However, the values mentioned in Tab. 9 for GJ 51 should be considered cautiously as our data sets provide a weak constraint and the resulting magnetic maps are largely determined by the entropy function used. In particular, the high values of longitudinal field measured (see Tab. 2) indicate that the large-scale magnetic flux is indeed higher than those of mid-M dwarfs studied in M08b. But it is not clear whether the large-magnetic flux of GJ 51 is actually larger than that of WX UMa (see Sec. 7). A definite confirmation of the magnetic topology of GJ 51 requires multi-site observations to obtain a complete sampling of the rotation cycle due to a period close to 1 d.

5 GJ 1156

We carried out 3 observing run on the flare star GJ 1156 — in 2007, 2008 and 2009 — and obtained 20 pairs of Stokes I and V spectra. The resulting LSD polarised signature is above noise level in nearly all observations. Tem-

Table 4. Same as Tab. 3 for GJ 1156.

Epoch	ℓ_{ZDI}	χ_{r0}^2	χ_{rf}^2	$\langle B \rangle$ (kG)	B_{max} (kG)
2007	6	1.95	0.95	0.06	0.32
2008	6	2.45	1.00	0.10	0.36
2009	6	2.07	1.00	0.09	0.36

poral variation is obvious on Figure 3, we observe both variations of amplitude and polarity. We use $v \sin i = 17 \text{ km s}^{-1}$ (Reiners & Basri 2007) which allows us to fit the observed polarised and unpolarised profiles, as opposed to the previously reported value ($v \sin i = 9.2 \text{ km s}^{-1}$, Delfosse et al. 1998). We derive $P_{rot} = 0.491 \text{ d}$, although $1/3 \text{ d}$ cannot be excluded as a possible period. This is confirmed by MEarth photometric periodogram which also exhibits a main peak at 0.491 d and another one at $1/3 \text{ d}$ (J. Irwin, private communication). The corresponding $R \sin i$ is $0.16 R_{\odot}$. As evolutionary models predict $R_{*} = 0.16 R_{\odot}$, we set $i=60^{\circ}$ for ZDI. The rotation period being close to a fraction of day our observations (especially those of 2007) do not provide an optimal sampling of rotation phases, only our 2008 data set provides a reasonable sampling on more than half of the rotation cycle.

The data sets can be fitted down to noise level with ZDI for the 3 epochs of observation (see Tab. 4). The corresponding maps of surface magnetic flux are displayed in

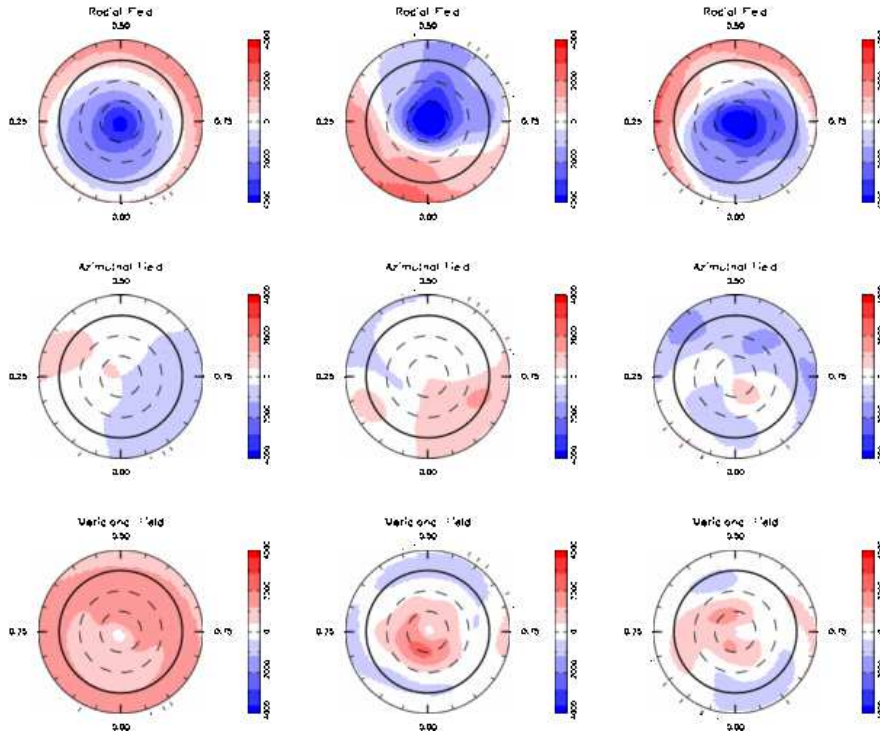


Figure 2. Surface magnetic flux of GJ 51 as derived from our 2006, (left-hand column), 2007 (middle column) and 2008 (right-hand column) data sets. For GJ 51, the imaging process is adapted to preferentially converge toward a mostly axisymmetric solution in order to resolve the ambiguity due to poor phase coverage (see text). The three components of the field in spherical coordinates are displayed from top to bottom (flux values labelled in G). The star is shown in flattened polar projection down to latitudes of -30° , with the equator depicted as a bold circle and parallels as dashed circles. Radial ticks around each plot indicate phases of observations.

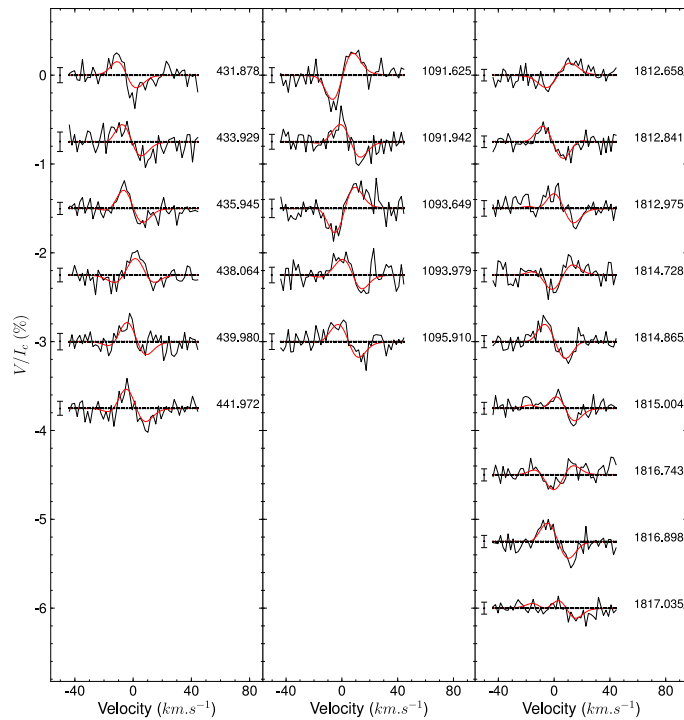


Figure 3. Same as Fig. 1 for GJ 1156 2007, 2008, and 2009 data sets (from left to right).

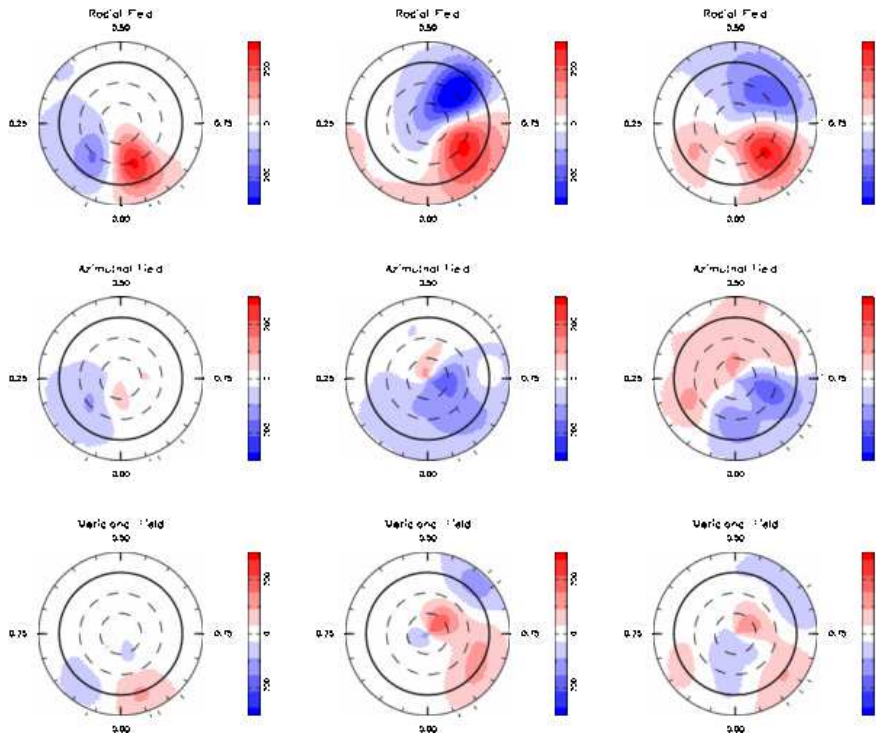


Figure 4. Same as Fig. 2 for GJ 1156 2007, 2008, and 2009 data sets (from left to right).

Figure 4. The 3 maps exhibit similar properties: they mainly feature two radial field spots of opposite polarities. The magnetic topologies are thus predominantly poloidal (more than 80 % of the overall magnetic energy in poloidal modes at all epochs) but feature a significant toroidal component (in particular in 2007 and 2008), and non-axisymmetric (more than 80 % of the overall magnetic energy in modes with azimuthal number $m > \ell/2$) as was expected from the polarity reversal of the V signature inside each data set. The lower average magnetic flux, as well as the weakness of the spot of negative polarity (incoming field lines, in blue), on the 2007 map can be attributed to poor phase coverage.

The reconstructed maps are quite robust to uncertainties on the input parameters (see Sec. 3.4). In particular, when varying these parameters, the fraction of magnetic energy reconstructed in non-axisymmetric modes ($m > \ell/2$) is always higher than 70%. Using the alternative values $P_{\text{rot}}=0.33$ d and $i=40^\circ$, the reconstructed magnetic maps do not change significantly. All the quantities listed in table 9 vary by less than 10 % of the total magnetic energy. The reconstructed magnetic flux variations range from 10 to 15 %. Considering these values therefore does not affect our conclusions.

6 GJ 1245 B

The M5.5 dwarf GJ 1245 B was observed during 3 successive years, for a total of 22 pairs of Stokes I and V spectra. The circularly polarised LSD signatures (see Fig. 5) have a moderate amplitude and exhibit strong variability (amplitude, shape and polarity) during an observation run — presumably due to rotational modulation. Variability also

Table 5. Same as Tab. 3 for GJ 1245 B.

Epoch	ℓ_{ZDI}	$\chi_{r_0}^2$	$\chi_{r_f}^2$	$\langle B \rangle$ (kG)	B_{max} (kG)
2006	4	4.41	1.00	0.17	0.47
2007	4	4.92	1.10	0.18	0.58
2008	4	1.81	1.00	0.06	0.22

seems important between the different epochs, in particular in the 2009 data set the average amplitude of the signatures is significantly lower than at previous epochs, this is also visible in the longitudinal field measurements (see Tab. 2).

We measure a mean $RV = 5.4$ km s $^{-1}$ with typical dispersions of 0.1 km s $^{-1}$ (see Tab. 2). This is compatible with the mean value of 5 km s $^{-1}$ reported by Delfosse et al. (1998). We use $v \sin i = 7$ km s $^{-1}$ (Delfosse et al. 1998 ; Reiners & Basri 2007); and find a rotation period of 0.71 d corresponding to a peak in the photometric periodogram produced by the HATNet² survey (J. Hartman, private communication). With these values of $v \sin i$ and period, we find $R \sin i = 0.10 R_\odot$, as the NextGen evolutionary model predicts $R_\star = 0.14 R_\odot$ we set $i = 40^\circ$ for our study.

Running ZDI on the LSD time-series, with the aforementioned parameters, we can achieve a good fit for the 3 epochs (see Fig. 5 and Tab. 5). The reconstructed magnetic field significantly evolves between two successive epochs, in particular the reconstructed magnetic flux has strongly decreased between our 2008 and 2009 observations. However

² Bakos et al. (2004)

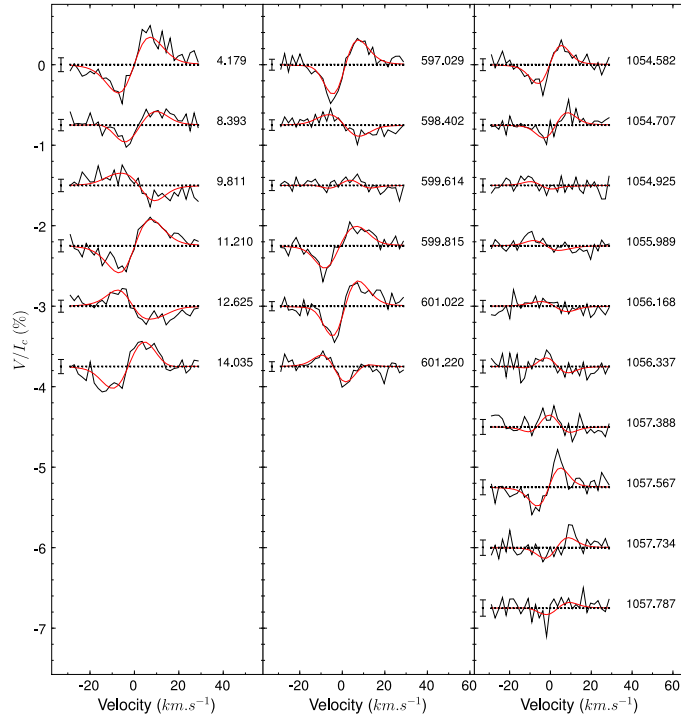


Figure 5. Same as Fig. 1 for GJ 1245 B 2006, 2007, and 2008 data sets (from left to right).

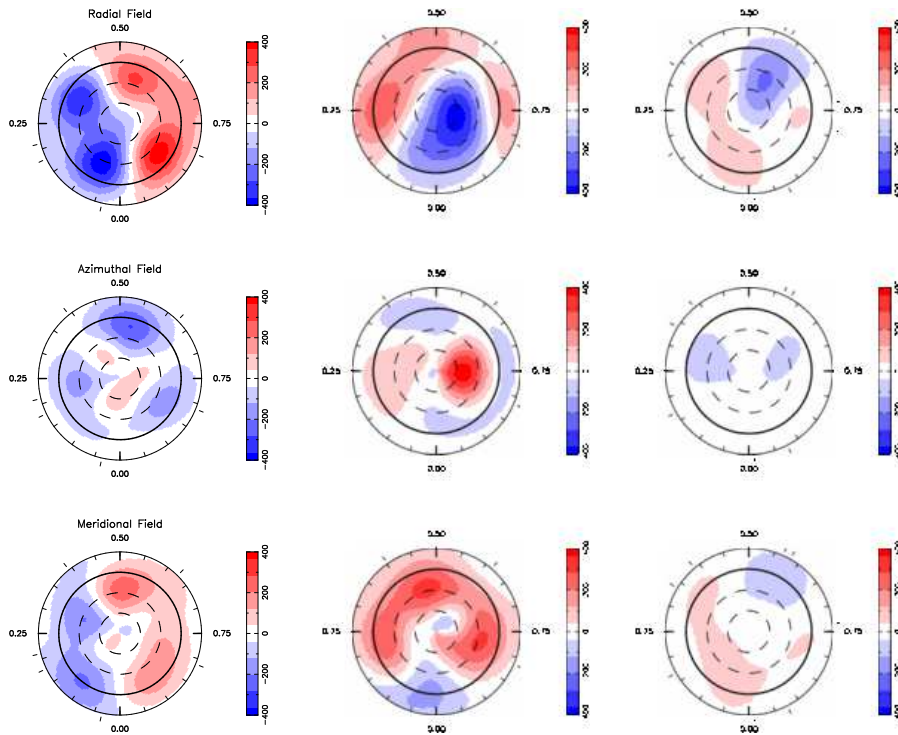


Figure 6. Same as Fig. 2 for GJ 1245 B 2006, 2007, and 2008 data sets (from left to right).

Table 6. Same as Tab. 3 for WX UMa.

Epoch	ℓ_{ZDI}	χ_{r0}^2	χ_{rf}^2	$\langle B \rangle$ (kG)	B_{max} (kG)
2006	4	8.98	0.90	0.89	3.82
2007	4	20.48	1.05	0.94	4.88
2008	4	12.42	1.00	1.03	4.55
2009	4	14.58	1.15	1.06	4.53

the magnetic topologies feature similar properties: strong spots of radial field (although more than 40 % of the magnetic energy lies in non-radial field structures); a mostly non-axisymmetric field (more than 50% of the magnetic energy) and a significant toroidal component (between 15 and 20% of the total magnetic energy). The mainly non-axisymmetric nature of the magnetic field in 2006 and 2008, as well as the presence of a significant toroidal component at all epochs are robust to uncertainties on stellar parameters (see Sec. 3.4).

7 WX UMA=GJ 412 B

Between 2006 and 2009, we observed the M6 dwarf WX UMa during 4 runs, collecting a total of 29 spectra. The LSD Stokes V profiles are very similar throughout the data set: a very strong (the peak-to-peak amplitude is close to 2% of the unpolarised continuum level) simple two-lobbed signature of negative polarity (i.e. corresponding to a longitudinal field directed toward the star). Temporal evolution inside each data set, presumably due to rotational modulation, is noticeable though weaker than what we observe on GJ 51. We measure average values ranging from $RV = 69.95$ to 70.25 km s^{-1} with a jitter ranging from 0.06 to 0.53 km s^{-1} (depending on the observation epoch, see Tab. 2). This is in agreement with $RV = 68.886 \text{ km s}^{-1}$ (single precise measurement by Nidever et al. 2002, on GJ 412A). We use $v \sin i = 5.0 \text{ km s}^{-1}$ (Reiners et al. 2009) which accounts for Zeeman broadening and results in better agreement with our Stokes I and V LSD profiles than the previous value of $v \sin i = 7.7 \text{ km s}^{-1}$ inferred from correlation profiles (Delfosse et al. 1998). From the circularly polarised LSD profiles we infer $P_{rot} = 0.74 \text{ d}$. With this rotation period, our 2007 data cover half of the rotation cycle, and the 3 other data sets result in a good phase coverage. The comparison of the resulting $R \sin i = 0.073 R_{\odot}$ with $R_{\star} = 0.12 R_{\odot}$ (from theoretical models) indicates an intermediate inclination angle, we set $i = 40^{\circ}$.

Although only the 2006 data set can be fitted below $\chi_r^2 = 1.0$ (see Tab. 6), the ZDI synthetic Stokes V profiles match well the evolution of the LSD signatures for all epochs, as shown in Fig. 7. The corresponding magnetic maps are presented in Fig. 8: they all feature a strong polar cap of radial field (of negative polarity, i.e. field lines directed toward the star) reaching a maximum flux of approximately 4 kG, whereas the magnetic flux averaged over the visible fraction of the star is about 1 kG. Azimuthal and meridional field structure are much weaker. The topology is very simple, modes with degree $\ell > 4$ can be neglected, the dipole modes encompass more than 60% of the reconstructed energy at all epochs. Toroidal and non-axisymmetric components of the

Table 7. Same as Tab. 3 for DX Cnc.

Epoch	ℓ_{ZDI}	χ_{r0}^2	χ_{rf}^2	$\langle B \rangle$ (kG)	B_{max} (kG)
2007	6	1.70	1.00	0.11	0.22
2008	6	1.42	1.00	0.08	0.20
2009	6	1.37	1.00	0.08	0.18

field are very weak. The evolution of the magnetic field over successive years is very weak, the maps are strikingly similar. These conclusions are robust to uncertainties on stellar parameters (in particular i and $v \sin i$). When varying these parameters over the width of their respective error bars (see section 3.4) the reconstructed magnetic field of WX UMa is always almost purely poloidal, mostly axisymmetric, and the main mode is the radial component of a dipole aligned with the rotation axis.

8 DX CNC=GJ 1111

We carried out 3 observation runs on DX Cnc between 2007 and 2009, resulting in 21 pairs of Stokes I and V spectra. The LSD polarised profiles are displayed in Fig. 9, the Zeeman signatures have low amplitudes but are definitely detected in several spectra. The amplitude and shape of the circularly polarised line dramatically evolve during each observing run, presumably due to rotational modulation. From the LSD profiles, we measure average RV ranging from 10.44 to 10.67 km s^{-1} , with a jitter strongly depending on the observing epoch (see Tab. 2), in agreement with the previously published values ($RV = 9 \text{ km s}^{-1}$ in Delfosse et al. 1998; $RV = 10.1 \text{ km s}^{-1}$ in Mohanty & Basri 2003). We use $v \sin i = 13 \text{ km s}^{-1}$ (Reiners & Basri 2007), and $P_{rot} = 0.46 \text{ d}$ (inferred from our data). As the resulting $R \sin i = 0.12 R_{\odot}$ is already higher than $R_{\star} = 0.11 R_{\odot}$ predicted by theoretical models, we assume a high inclination angle of the rotation axis and set $i = 60^{\circ}$ for the imaging process. Our 2007 and 2008 data sets provide a reasonable phase coverage and the 2009 one results in a good sampling of the stellar rotation.

Both the mean longitudinal field and the standard deviation from this value get weaker from one observing run to the next one, indicating intrinsic variability of the magnetic field. Using the ZDI tomographic imaging code, we can fit the 3 data sets down to $\chi_r^2 = 1.0$, the resulting magnetic fields are presented in Fig. 10. Although for the three epochs, the reconstructed magnetic topologies feature a significant non-axisymmetric component, they significantly differ from each other: (i) the fraction of magnetic energy reconstructed in the toroidal component grows from 7% in 2007 to 38% in 2009; (ii) the two main spots of radial magnetic field seem to evolve between 2007 and 2008, and finally in 2009 only one region of strong radial field remains. (iii) The averaged magnetic flux decreases from 110 G in 2007 to 80 G in 2008 and 2009. This last point is strengthened by the fact that for a given topology, ZDI recovers less magnetic flux for a dataset providing partial phase coverage (due to the maximum entropy constraint), whereas here the larger flux is

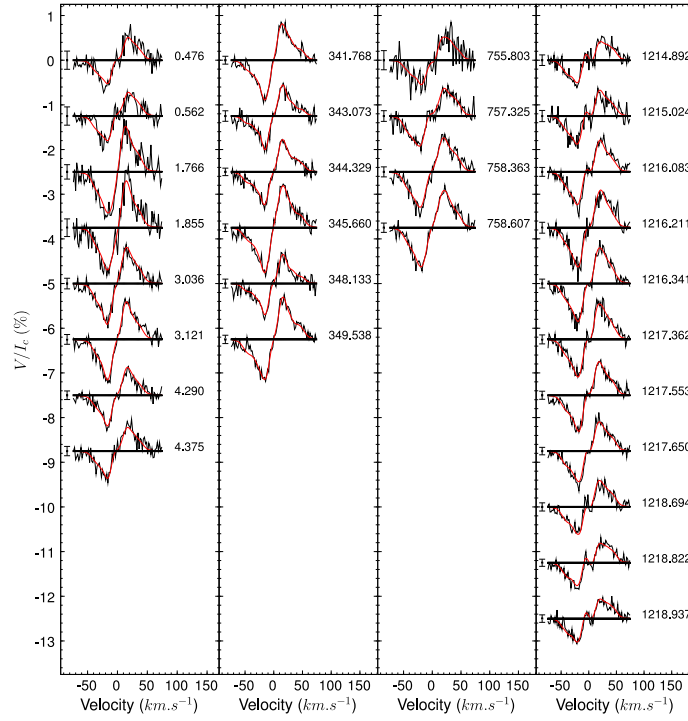


Figure 7. Same as Fig. 1 for WX UMa 2006, 2007, 2008 and 2009 data sets (from left to right).

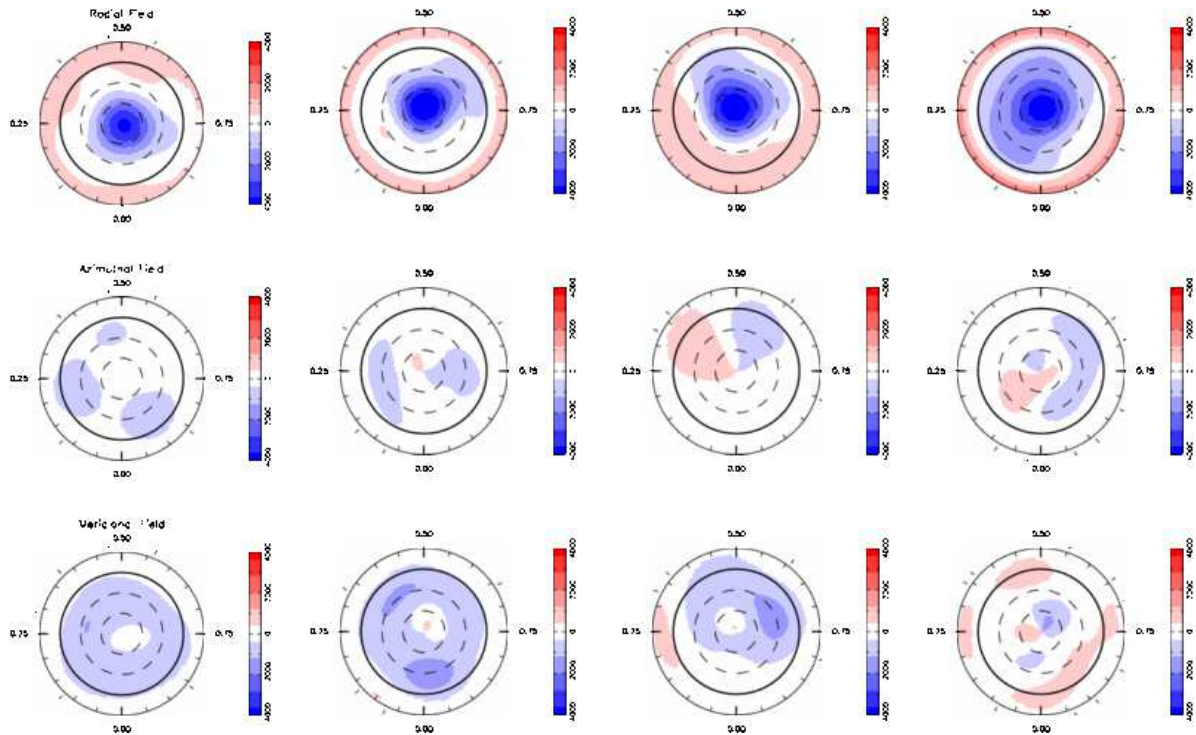


Figure 8. Same as Fig. 2 for WX UMa 2006, 2007, 2008 and 2009 data sets (from left to right).

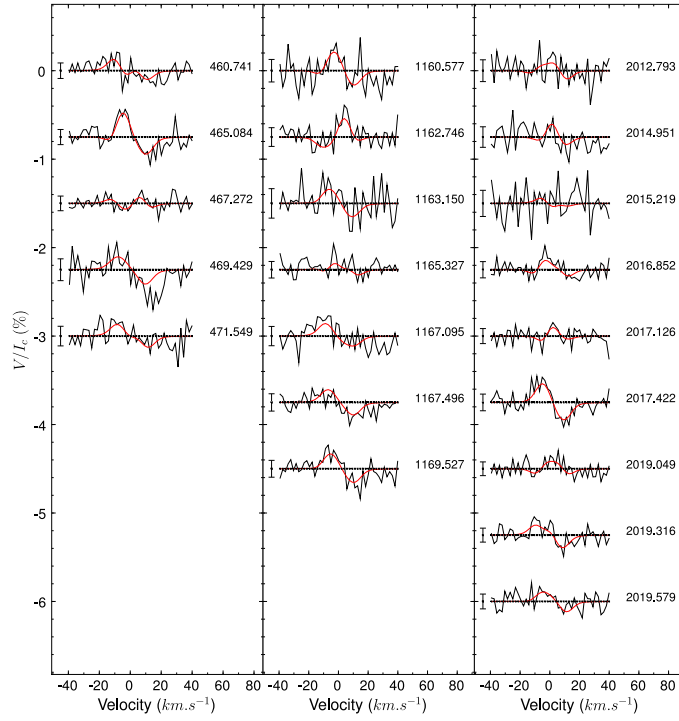


Figure 9. Same as Fig. 1 for DX Cnc 2007, 2008, and 2009 data sets (from left to right).

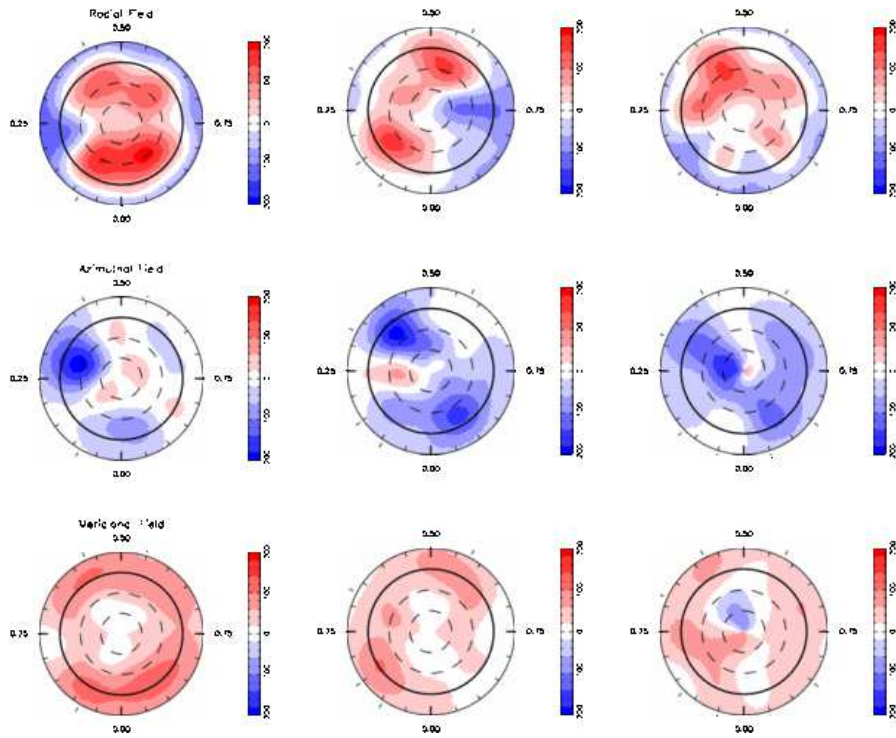


Figure 10. Same as Fig. 2 for DX Cnc 2007, 2008, and 2009 data sets (from left to right).

Table 8. Same as Tab. 3 for GJ 3622.

Epoch	ℓ_{ZDI}	χ_{r0}^2	χ_{rf}^2	$\langle B \rangle$ (kG)	B_{max} (kG)
2008	2	2.08	0.95	0.05	0.11
2009	2	1.68	0.95	0.06	0.11

inferred from the dataset providing the poorest sampling of stellar rotation. The presence of a strong toroidal component on DX Cnc in 2008 and 2009 is a robust result. In particular, when varying the input parameters within their respective error bars (see Sec. 3.4) the toroidal component always accounts for at least 30 % of the reconstructed magnetic energy.

9 GJ 3622

GJ 3622 was observed in 2008 and 2009, we collected 8 and 5 sequences, respectively. In spite of relatively low S/N (due to a low intrinsic luminosity), Stokes V signatures are clearly detected in several spectra and variations are undoubtedly noticeable (see Fig. 11). From our data sets we infer $P_{rot} = 1.5$ d, and use $v \sin i = 3 \text{ km s}^{-1}$ reported by Mohanty & Basri (2003), resulting in $R \sin i = 0.09 R_{\odot}$. Our data sets provide a reasonable phase coverage with this period. As evolutionary models predict $R_{\star} = 0.11 R_{\odot}$ for a $0.09 M_{\odot}$ M dwarf, we set the inclination angle to 60° for the imaging process.

Setting $\ell_{max} = 2$, given the very weak signal detected, it is possible to fit our 2 data sets down to noise level (see Tab. 8). The corresponding magnetic maps (see Fig. 11) are very similar. A radial field spot of negative polarity, i.e. field lines directed toward the star, is located at mid-latitudes. Magnetic flux reaches up to 110 G in this region. Azimuthal and meridional fields are much weaker, the toroidal component represents less than 10 % of the overall magnetic energy at both epochs. The reconstructed topology is close to a tilted dipole: less than 10 % of the magnetic energy is reconstructed in $\ell = 2$ modes, and the axisymmetric component stands for more than 80 % of the energy content. The data being very noisy the simple topology reconstructed by ZDI likely reflects the lack of information in the polarised spectra.

10 OTHER STARS

For five stars of our sample we collected time series of polarised spectra but could not produce a definitive magnetic map. For GJ 1154 A, GJ 1224 and CN Leo (GJ 406) we detect very strong and simple signatures (see Fig. 12). To our knowledge, no rotation periods have been measured for these stars and our data sets do not allow us to conclude, either because of low intrinsic variability of the Zeeman signature or poor phase sampling. Although we cannot compute a magnetic map for these stars, the collected spectra unmistakably show that they host very strong large-scale magnetic fields (longitudinal fields are about 600 G). Strong magnetic fields

(total magnetic fluxes in the 2-3 kG range) have been previously detected on these stars by Reiners & Basri (2007) and Reiners et al. (2009) from the analysis of unpolarised spectra (see Tab. 1). The simple signatures (two-lobbed anti-symmetric) featuring very low variability also clearly suggest that these fields are mostly poloidal, strongly axisymmetric and presumably dominated by low degree modes, similar to what we observe on GJ 51 and WX UMa for instance. The low dispersions of longitudinal fields and RV values in each data set may indicate that phase sampling is loose and thus rotation period close to a fraction of day, or/and that these stars are observed nearly pole-on.

For the faintest stars of the sample VB 8 (GJ 644 C) and VB 10 (GJ 752 B), the Stokes V signatures are too weak to be definitely detected in individual LSD spectra. The initial χ_{r0}^2 are respectively equal to 1.089 and 1.150. LSD signatures observed on these stars are shown on Figure 13. By averaging all the LSD profiles of a data set, the noise level is decreased but only features visible on all spectra — corresponding to the axisymmetric component of the field, if rotation sampling is even — remain visible. The resulting signal shown in Fig. 13 (bold red line) is processed with a zero phase shift low-pass filter to remove the frequencies higher than permitted by the instrumental profile (width of 4.6 km s^{-1} , or 2.5 LSD pixels). For VB 8, the averaged LSD profile does not feature any significant signal ($\chi_r^2=0.99$), indicating that the axisymmetric component of the magnetic field of this star is too weak to be detected. The averaged profile of VB 10 features a weak but distinguishable signature corresponding to $\chi_r^2 = 1.90$. It suggests the presence of a large-scale magnetic field having a significant axisymmetric component, but further observations are needed to confirm this point. From observations in unpolarised light, Reiners & Basri (2007) report total magnetic fluxes of 2.3 and 1.3 kG on VB 8 and VB 10, respectively (see Tab. 1). The very weak Stokes V signatures observed here (with corresponding maximum longitudinal fields of the order of 100 G) suggest that the magnetic field of these stars is mainly structured on small spatial scales.

Performing a ZDI analysis on the VB 10 time series, we find 2 possible rotation periods: 0.52, and 0.69 d, the second being favored by photometric measurements (MEarth project, J. Irwin, private communication). Figure 14 shows the fit achieved for $P_{rot} = 0.69$ d, $i = 60^{\circ}$ and the corresponding magnetic maps. As expected from the signature shape (non antisymmetric with respect to the line centre), the reconstructed magnetic field exhibits a significant axisymmetric toroidal component. A non-axisymmetric poloidal field (tilted quadrupole, mode α_{22}) is also reconstructed to fit the Stokes V component that varies along rotation.

11 DISCUSSION AND CONCLUSION

We present the final part of our exploratory spectropolarimetric survey of M dwarfs, following D08 and M08b (respectively concentrating on mid and early M dwarfs) we focus here on the low mass end of our sample. For 6 stars, it is possible to apply ZDI techniques to the time-series of circularly polarised spectra and thus to infer the large-scale component of their magnetic topologies. The properties of

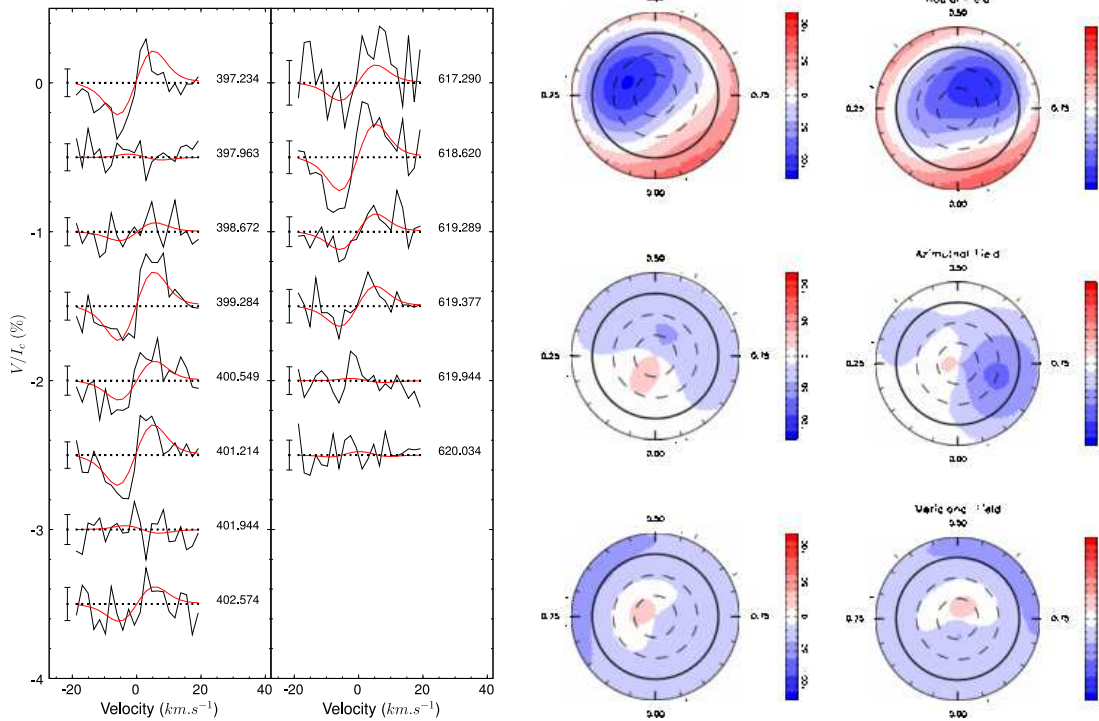


Figure 11. 2008 and 2009 spectra and magnetic maps of GJ 3622. See Fig. 1 and 2 for more details.

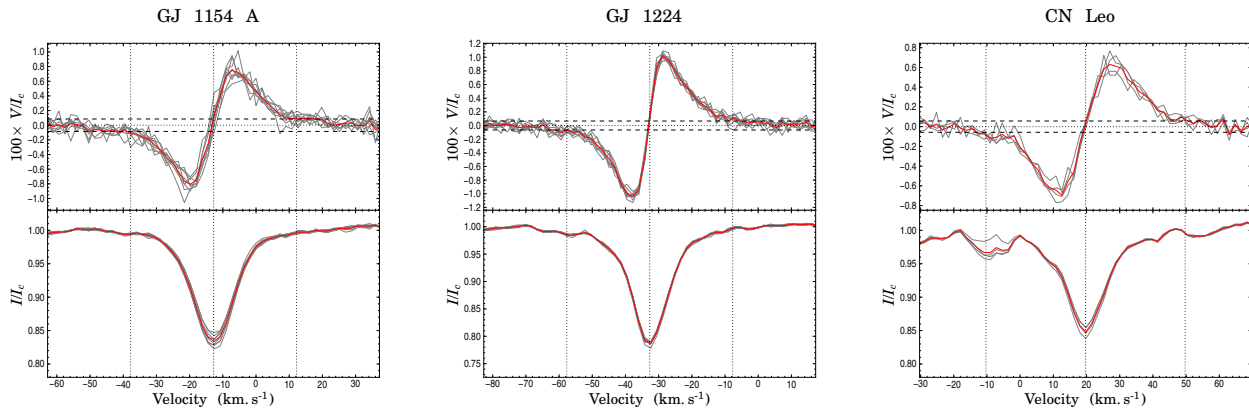


Figure 12. Stokes I (lower panels) and V (upper panels) LSD signatures of GJ 1154 A, GJ 1224 and CN Leo, from left to right. In each panel all the profiles of the time series are plotted as superimposed grey lines, and the average profile is shown in red. Vertical dotted lines represent the line center (in bold) and the approximate limits of the line. In Stokes V plots $\pm 1\sigma$ levels (corresponding the individual spectra) are shown as dashed lines, and the reference level as a dotted line.

the reconstructed topologies of these stars are presented in Table 9. For the remaining 5 objects, the data sets do not permit such a study, it is however possible to retrieve some constraints about their magnetic properties.

Two stars of the subsample (namely GJ 51 and WX UMa) exhibit large-scale magnetic fields very similar to those observed by M08b on mid M dwarfs, i.e. very strong, axisymmetric poloidal and nearly dipolar fields, with very little temporal variations. For three stars for which we cannot perform a definitive ZDI reconstruction (GJ 1154 A, GJ 1224 and CN Leo) our data strongly suggest similar topologies. From the observations of WX UMa, we demon-

strate that the timescale of temporal evolution in the magnetic topologies of these stars can be larger than 3 years, whereas previous observations by M08a and M08b were based on observations spanning only 1 year.

The other stars for which we can reconstruct the large-scale magnetic topologies, are clearly different. They are weaker than those of the first category, and generally feature a significant non-axisymmetric component, plus a significant toroidal component (although the field is always predominantly poloidal). Temporal variability is also noticeable, in particular for GJ 1245 B our data indicate unambiguously that the magnetic field strength has dramatically decreased

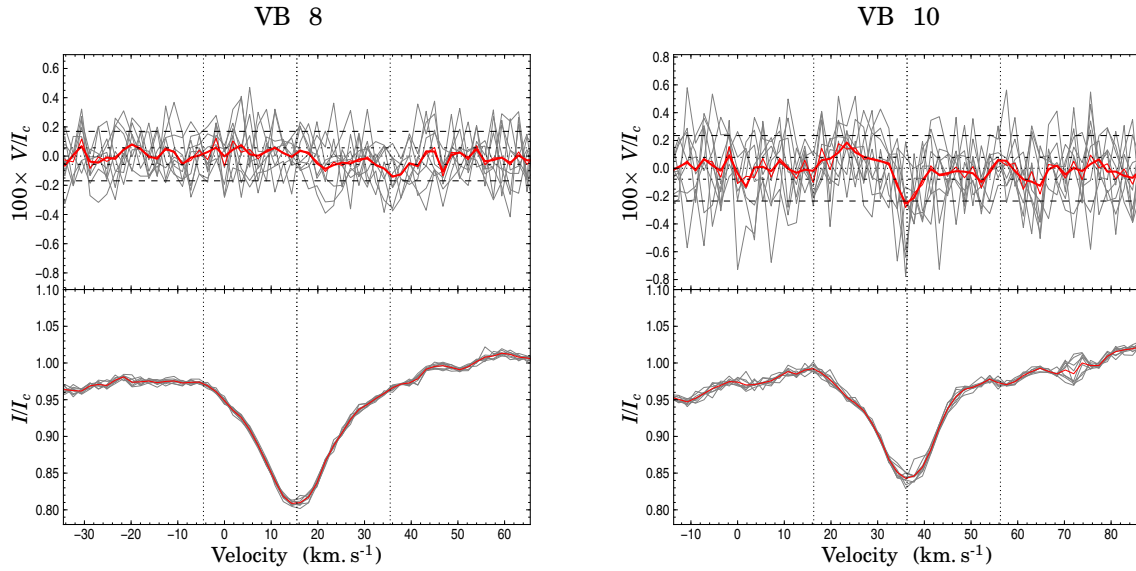


Figure 13. Same as Fig. 12 for VB 8 and VB 10. The bold red line results from low-pass filtering of the Stokes V signatures and dash-dotted lines show the $\pm 1\sigma$ levels corresponding the averaged spectra.

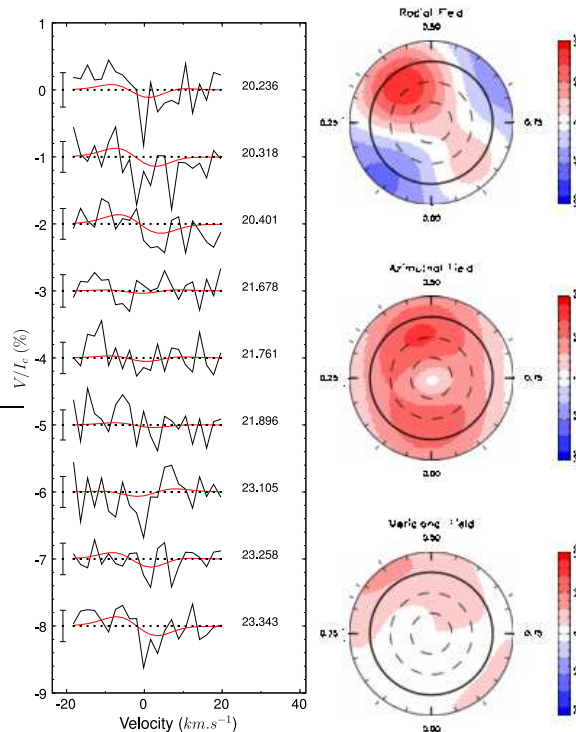


Figure 14. 2009 spectra and magnetic maps of VB 10. See Fig. 1 and 2 for more details. Data are phased according to the ephemeris $\text{HJD} = 2\,455\,000 + 0.69 E$.

between our 2007 and 2008 observations. Our conclusions are robust to uncertainties on stellar parameters (P_{rot} , i and $v \sin i$). When varying these parameters over the width of their respective error bars (see section 3.4), the main properties of the reconstructed magnetic topologies remain unchanged.

These results are presented in a more visual way in Fig. 15. Previous studies by D08 and M08b have revealed

strong evidence that a clear transition occurs at approximately $0.5 M_{\odot}$ i.e. more or less coincident with the transition to a fully convective internal structure. The situation here is different, we find stars with similar stellar parameters that exhibit radically different magnetic topologies. On Fig. 15, WX UMa is the only star below $0.2 M_{\odot}$ to host a mid-M-dwarf-like field. Whereas DX Cnc and GJ 1245 B are very close to it in the mass-rotation plane they feature

Table 9. Magnetic quantities derived from our study. For each star, different observation epochs are presented separately. In columns 2–4 we report quantities from Table 1, respectively the stellar mass, the rotation period, and the effective Rossby number. Columns 5, 6 and 7 mention the Stokes V filling factor, the reconstructed magnetic energy and the average magnetic flux. Columns 8–11 list the percentage of reconstructed magnetic energy respectively lying in poloidal, dipole (poloidal and $\ell = 1$), quadrupole (poloidal and $\ell = 2$), and octupole (poloidal and $\ell = 3$) modes. In column 12, we mention the percentage of magnetic energy reconstructed in axisymmetric modes (defined as $m < \ell/2$) and the percentage of poloidal energy in axisymmetric modes. See section 3.4 for a discussion on the robustness of magnetic map reconstruction and the uncertainties associated with the derived quantities.

Name	Mass (M_{\odot})	P_{rot} (d)	Ro (10^{-2})	f_V	$\langle B^2 \rangle$ (10^5 G^2)	$\langle B \rangle$ (kG)	pol. (%)	dipole (%)	quad. (%)	oct. (%)	axisymm. (%)
GJ 51 ¹ (06)	0.21	1.02	1.2	0.12	38.6	1.61	99	96	0	2	91/91
(07)	–	–	–	0.12	31.3	1.58	99	92	0	6	77/77
(08)	–	–	–	0.12	32.6	1.65	97	92	1	3	89/89
GJ 1156 ² (07)	0.14	0.49	0.5	1.0	0.06	0.05	88	30	26	19	6/3
(08)	–	–	–	1.0	0.19	0.11	83	41	28	11	20/12
(09)	–	–	–	1.0	0.13	0.10	94	54	24	10	2/1
GJ 1245 B (06)	0.12	0.71	0.7	0.06	0.44	0.17	80	45	14	13	15/9
(07)	–	–	–	0.10	0.49	0.18	84	46	27	7	52/53
(08)	–	–	–	0.10	0.06	0.06	85	33	25	19	20/18
WX UMa (06)	0.10	0.78	0.8	0.12	16.08	0.89	97	66	21	6	92/92
(07)	–	–	–	0.12	24.42	0.94	97	71	13	3	92/94
(08)	–	–	–	0.12	23.53	1.03	97	69	19	6	83/85
(09)	–	–	–	0.12	37.54	1.06	96	89	2	2	95/96
DX Cnc (07)	0.10	0.46	0.5	0.20	0.17	0.11	93	69	11	9	77/77
(08)	–	–	–	0.20	0.09	0.08	73	31	25	10	49/34
(09)	–	–	–	0.20	0.09	0.08	62	42	11	4	70/61
GJ 3622 (08)	0.09	1.5	1.5	1.0	0.04	0.05	96	90	7	–	73/72
(09)	–	–	–	1.0	0.05	0.06	93	84	9	–	80/78

¹ For GJ 51, the imaging process is weakly constrained by our data sets due to poor phase coverage (see Sec. 4).

² For GJ 1156 the alternative rotation period 0.33 d cannot be definitely excluded (see Sec. 5). In this case, the reconstructed topologies remain similar for the 3 epochs, and our conclusions are not affected.

fields with very different properties. This observation may be explained in several ways. For instance, another parameter than mass and rotation period, such as stellar age, may play a role. In our sample we indeed notice that most stars below $0.15 M_{\odot}$ that exhibit a weak complex field belong to a young kinematic population according to Delfosse et al. 1998 (GJ 1156, DX Cnc and GJ 3622), whereas those hosting a strong dipolar field (WX UMa, GJ 1224 and CN Leo) belong to older kinematic populations (old disk and old/young disk). This hypothesis requires further investigation. One could also imagine, for instance, that the magnetic fields of very low mass stars may switch between two different states over time. This hypothesis is supported by the fact that for one of the stars in the weak and complex field regime (GJ 1245 B) we observe a dramatic variation of the magnetic flux on a timescale of one year which may indicate that the magnetic field of these objects may go through chaotic variations and eventually switch between the two categories of field actually observed. However no such switch has been observed in our sample. We observe 5 objects in the strong dipole field category (GJ 51, GJ 1154 A, GJ 1224, CN Leo and WX UMa) and 6 in the weak field category (GJ 1156, GJ 1245 B, DX Cnc, GJ 3622, VB 8 and VB 10), indicating that stars would spend as much time in both states. No star is observed in an intermediate state, suggesting that a putative transition would be fast. This hypothesis may be investigated through the analysis of long-term radio monitoring, since radio emission would be presumably strongly

impacted by such a dramatic change of the stellar magnetic field. Recent observations of ultracool dwarfs reveal a long-term variability of the activity indices (e.g., Antonova et al. 2007; Berger et al. 2010) that may support this view.

On the left panel of Fig. 16, we plot the reconstructed magnetic flux as a function of the Rossby number. As mentioned in D08, stars with $M_{\star} > 0.4 M_{\odot}$ follow the expected rotation–magnetic field connection, with saturation for $Ro \lesssim 0.2$. Whereas for $M_{\star} > 0.4 M_{\odot}$, we only observe objects in the saturated regime, with a significantly stronger saturation magnetic flux. All the stars of the late M subsample have Rossby numbers below 2×10^{-2} and are thus expected to be in the saturated regime. As in Fig. 15 the stars studied here can be divided into two distinct categories. The first one is composed of stars hosting a very strong magnetic field that lie in the saturated part of the rotation–activity relation, similar to mid M dwarfs. We notice that significantly higher magnetic fluxes are reconstructed for WX UMa and GJ 51 than for mid M dwarfs studied by M08b, although all these stars seem to lie in the saturated dynamo regime. For the second category of late M dwarfs (having a weak complex field), we recover less magnetic flux (even less than for some early M dwarfs studied by D08), in spite of their very low Rossby number. Super-saturation is unlikely to be the explanation since stars of both categories have similar Rossby numbers. As mentioned for Fig. 15, we observe no object in an intermediate state. The aforementioned variability of GJ 1245 B is also prominent in this plot.

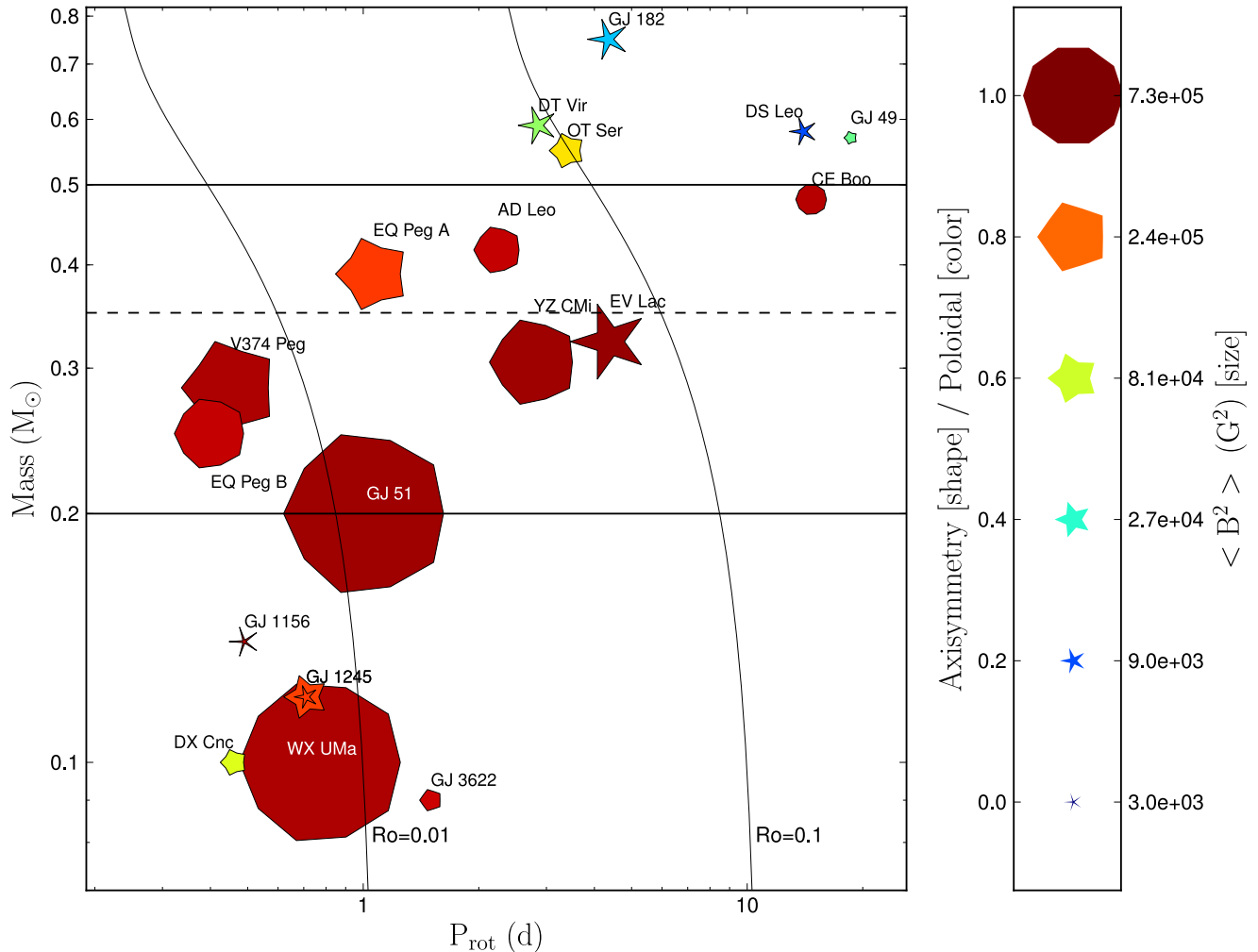


Figure 15. Properties of the magnetic topologies of our sample of M dwarfs as a function of rotation period and stellar mass. Larger symbols indicate larger magnetic fields while symbol shapes depict the different degrees of axisymmetry of the reconstructed magnetic field (from decagons for purely axisymmetric fields to sharp stars for purely non axisymmetric fields). Colours illustrate the field configuration (dark blue for purely toroidal fields, dark red for purely poloidal fields and intermediate colours for intermediate configurations). Solid lines represent contours of constant Rossby number $Ro = 0.1$ and 0.01 respectively corresponding approximately to the saturation and super-saturation thresholds (e.g., Pizzolato et al. 2003). The theoretical full-convection limit ($M_* \simeq 0.35M_\odot$, Chabrier & Baraffe 1997) is plotted as a horizontal dashed line, and the approximate limits of the three stellar groups discussed in the text are represented as horizontal solid lines. Stars with $M_* > 0.45 M_\odot$ are from D08, whereas those with $0.25 < M_* < 0.45 M_\odot$ are from M08b. For GJ 1245 B symbols corresponding to 2007 and 2008 data sets are superimposed in order to emphasize the variability of this object. Uncertainties associated with the plotted magnetic quantities are discussed in section 3.4.

On the right panel of Fig. 16, magnetic flux inferred from Stokes V measurements is compared to those derived from Stokes I . Again, stars with masses below and above $0.4 M_\odot$ studied by D08 and M08b clearly form two separate groups. In partly-convective stars only a few percents of the magnetic flux measured in I is detectable in V similarly to what is observed for the Sun, while this ratio is close to 15% in fully convective ones. This indicates a higher degree of organization of the field in fully convective mid M dwarfs, with more magnetic flux in the spherical harmonics of lowest degree. The ratios of about 30% plotted for WX UMa are upper limits (since the flux based on Stokes I is a lower limit), it is thus not clear if this star differs from mid M dwarfs in this respect. This high value however indicates a

high degree of organization. For DX Cnc, GJ 1245 B and GJ 1156, the ratio of Stokes V and I fluxes is closer to the early M dwarfs value. Therefore the magnetic fields of the weak field category of late M dwarfs share similar properties with that of partly convective M dwarfs.

These results on the magnetic topologies of M dwarfs also suggest that dynamo processes in low-mass main sequence stars and pre-main sequence stars may be similar. Indeed the first spectropolarimetric results on young stars show that the fully convective T Tauri star BP Tau ($0.7 M_\odot$) exhibit a strong large-scale magnetic field (Donati et al. 2008a), whereas the more massive partly convective star V2129 Oph ($1.4 M_\odot$) possesses a weaker and more complex field (Donati et al. 2007). This is reminiscent of the transi-

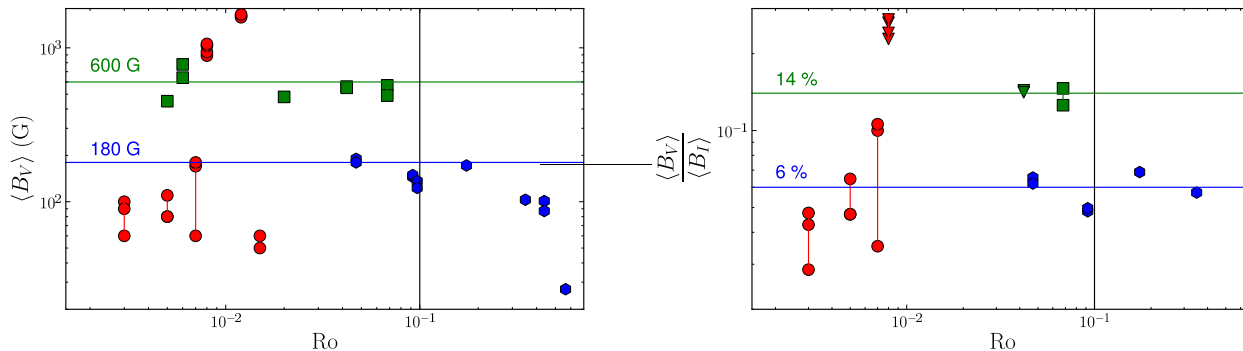


Figure 16. Magnetic flux as a function of Rossby number. On the left panel magnetic fluxes as measured from Stokes V spectra and ZDI by M08b and D08 are mentioned as blue hexagons ($M_\star > 0.4 M_\odot$) and green squares ($0.2 < M_\star < 0.4 M_\odot$). Results from this paper ($M_\star \leq 0.2 M_\odot$) are shown as red circles. On the right panel the ratio between the magnetic fluxes as recovered from Stokes V and Stokes I measurements (whenever available) are shown. Stokes I magnetic fluxes are taken from Johns-Krull & Valenti (2000), Reiners & Basri (2007), Reiners et al. (2009), and Reiners & Basri (2009) (see Tab. 1). Measurements of different epochs (whenever available) for Stokes V are shown connected by a solid line. On each plot the $Ro = 10^{-1}$, corresponding to the saturation level, is depicted as a vertical solid black line. Triangles denote upper limits. In the left panel, horizontal lines show the magnetic fluxes corresponding to saturation for stars with $M_\star > 0.4 M_\odot$ (blue), and $0.2 < M_\star < 0.4 M_\odot$ (green). In the right panel they show the mean fraction of magnetic flux detected in Stokes V spectra.

tion we observe at $0.5 M_\odot$ among main sequence M dwarfs. Recent observations, on the fully convective V2247 Oph ($0.35 M_\odot$) reveal a still weaker and more complex magnetic field (Donati et al. 2010) which may correspond to the weak field late M dwarf we present here.

We do not detect Stokes V signatures in individual spectra of the two latest stars of our sample VB 8 and VB 10. However the averaged LSD profile of VB 10 suggests the presence of a toroidal axisymmetric field component on this object. Further observations may confirm this first spectropolarimetric detection on an ultra-cool dwarf.

The first spectropolarimetric survey of M dwarfs has already provided dynamo theorists with strong constraints on the evolution of surface magnetic fields of M dwarfs across the fully convective divide (D08 and M08b). The results presented in this paper on the magnetic topologies of late M dwarfs reveal a new unexpected behaviour below $0.2 M_\odot$. We interpret the fact that objects with similar stellar parameters host radically different magnetic topologies as a possible evidence for a switch between two dynamo states (either cyclic or chaotic). Finally our observations suggest the presence of a large-scale magnetic field on the M8 dwarf VB 10, featuring a significant toroidal axisymmetric component, whereas the detection of the magnetic field of VB 8 (M7) is not possible from our spectropolarimetric data.

ACKNOWLEDGEMENTS

The authors thank the CFHT staff for their valuable help throughout our observing runs. We are grateful to Jonathan Irwin and Joel Hartman for providing results prior to publication on the photometric periods of the M dwarfs studied in this paper. We also thank the referee Gibor Basri for his fruitful suggestions.

REFERENCES

- Antonova A., Doyle J. G., Hallinan G., Golden A., Koen C., 2007, *A&A*, 472, 257
 Babcock H. W., 1961, *ApJ*, 133, 572
 Bakos G., Noyes R. W., Kovács G., Stanek K. Z., Sasselov D. D., Domsa I., 2004, *PASP*, 116, 266
 Baraffe I., Chabrier G., Allard F., Hauschildt P. H., 1998, *A&A*, 337, 403
 Berger E., 2006, *ApJ*, 648, 629
 Berger E., Basri G., Fleming T. A., Giampapa M. S., Gizis J. E., Liebert J., Martín E., Phan-Bao N., Rutledge R. E., 2010, *ApJ*, 709, 332
 Browning M. K., 2008, *ApJ*, 676, 1262
 Chabrier G., Baraffe I., 1997, *A&A*, 327, 1039
 Chabrier G., Küker M., 2006, *A&A*, 446, 1027
 Charbonneau P., 2005, *Living Reviews in Solar Physics*, 2, 2
 Cowling T. G., 1933, *MNRAS*, 94, 39
 Cutri R. M., Skrutskie M. F., van Dyk S., Beichman C. A., Carpenter J. M., Chester T., Cambresy L., Evans T., Fowler J., Gizis J., Howard E., Huchra J., Jarrett T., Kopan E. L., Kirkpatrick J. D., Light R. M., Marsh K. A., McCallon 2003, 2MASS All Sky Catalog of point sources.. The IRSA 2MASS All-Sky Point Source Catalog, NASA/IPAC Infrared Science Archive. [http://irsa.ipac.caltech.edu/applications/Gator/Delfosse X., Forveille T., Perrier C., Mayor M., 1998, *A&A*, 331, 581](http://irsa.ipac.caltech.edu/applications/Gator/Delfosse X., Forveille T., Perrier C., Mayor M., 1998, A&A, 331, 581)
 Delfosse X., Forveille T., Ségransan D., Beuzit J.-L., Udry S., Perrier C., Mayor M., 2000, *A&A*, 364, 217
 Demory B., Ségransan D., Forveille T., Queloz D., Beuzit J., Delfosse X., di Folco E., Kervella P., Le Bouquin J., Perrier C., Benisty M., Duvert G., Hofmann K., Lopez B., Petrov R., 2009, *A&A*, 505, 205
 Dobler W., Stix M., Brandenburg A., 2006, *ApJ*, 638, 336
 Donati J., Skelly M. B., Bouvier J., Jardine M. M., Gregory S. G., Morin J., Hussain G. A. J., Dougados C., Ménard F., Unruh Y., 2010, *MNRAS*, 402, 1426

- Donati J.-F., Brown S. F., 1997, *A&A*, 326, 1135
- Donati J.-F., Forveille T., Cameron A. C., Barnes J. R., Delfosse X., Jardine M. M., Valenti J. A., 2006a, *Science*, 311, 633
- Donati J.-F., Howarth I. D., Jardine M. M., Petit P., Catala C., Landstreet J. D., Bouret J.-C., Alecian E., Barnes J. R., Forveille T., Paletou F., Manset N., 2006b, *MNRAS*, 370, 629
- Donati J.-F., Jardine M. M., Gregory S. G., Petit P., Bouvier J., Dougados C., Ménéard F., Cameron A. C., Harries T. J., Jeffers S. V., Paletou F., 2007, *MNRAS*, 380, 1297
- Donati J.-F., Jardine M. M., Gregory S. G., Petit P., Paletou F., Bouvier J., Dougados C., Ménéard F., Cameron A. C., Harries T. J., Hussain G. A. J., Unruh Y., Morin J., Marsden S. C., Manset N., Aurière M., Catala C., Alecian E., 2008a, *MNRAS*, 386, 1234
- Donati J.-F., Morin J., Petit P., Delfosse X., Forveille T., Aurière M., Cabanac R., Dintrans B., Fares R., Gastine T., Jardine M. M., Lignières F., Paletou F., Velez J. C. R., Théado S., 2008b, *MNRAS*, 390, 545
- Donati J.-F., Semel M., Carter B. D., Rees D. E., Cameron A. C., 1997, *MNRAS*, 291, 658
- Durney B. R., De Young D. S., Roxburgh I. W., 1993, *Solar Physics*, 145, 207
- ESA 1997, *VizieR Online Data Catalog*, 1239, 0
- Gizis J. E., Reid I. N., Hawley S. L., 2002, *AJ*, 123, 3356
- Guedel M., Benz A. O., 1993, *ApJL*, 405, L63
- Horne K., 1986, *PASP*, 98, 609
- Irwin J., Charbonneau D., Nutzman P., Falco E., 2009, in E. Stempels ed., *American Institute of Physics Conference Series Vol. 1094 of American Institute of Physics Conference Series, The M-Earth project: searching for transiting habitable super-Earth planets around nearby M-dwarfs*. pp 445–448
- Johns-Krull C. M., Valenti J. A., 1996, *ApJL*, 459, L95+
- Johns-Krull C. M., Valenti J. A., 2000, in Pallavicini R., Micela G., Sciortino S., eds, *Stellar Clusters and Associations: Convection, Rotation, and Dynamos Vol. 198 of Astronomical Society of the Pacific Conference Series*, Measurements of stellar magnetic fields. pp 371–+
- Kiraga M., Stepien K., 2007, *Acta Astronomica*, 57, 149
- Küker M., Rüdiger G., 1999, *A&A*, 346, 922
- Kurucz R., 1993, *CDROM # 13 (ATLAS9 atmospheric models) and # 18 (ATLAS9 and SYNTHE routines, spectral line database)*. Smithsonian Astrophysical Observatory, Washington D.C.
- Larmor J., 1919, *Rep. Brit. Assoc. Adv. Sci.*
- Leighton R. B., 1969, *ApJ*, 156, 1
- Marsh T. R., 1989, *PASP*, 101, 1032
- Mohanty S., Basri G., 2003, *ApJ*, 583, 451
- Morin J., Donati J.-F., Forveille T., Delfosse X., Döbler W., Petit P., Jardine M. M., Cameron A. C., Albert L., Manset N., Dintrans B., Chabrier G., Valenti J. A., 2008a, *MNRAS*, 384, 77
- Morin J., Donati J.-F., Petit P., Delfosse X., Forveille T., Albert L., Aurière M., Cabanac R., Dintrans B., Fares R., Gastine T., Jardine M. M., Lignières F., Paletou F., Ramirez Velez J. C., Théado S., 2008b, *MNRAS*, 390, 567
- Moutou C., Donati J.-F., Savalle R., Hussain G., Alecian E., Bouchy F., Catala C., Collier Cameron A., Udry S., Vidal-Madjar A., 2007, *A&A*, 473, 651
- Nidever D. L., Marcy G. W., Butler R. P., Fischer D. A., Vogt S. S., 2002, *ApJS*, 141, 503
- Noyes R. W., Hartmann L. W., Baliunas S. L., Duncan D. K., Vaughan A. H., 1984, *ApJ*, 279, 763
- Ossendrijver M., 2003, in Pevtsov A. A., Uitenbroek H., eds, *Current Theoretical Models and Future High Resolution Solar Observations: Preparing for ATST Vol. 286 of Astronomical Society of the Pacific Conference Series*, The Solar Dynamo: A Challenge for Theory and Observations (Invited review). p. 97
- Parker E. N., 1955, *ApJ*, 122, 293
- Petit P., Dintrans B., Solanki S. K., Donati J., Aurière M., Lignières F., Morin J., Paletou F., Ramirez Velez J., Catala C., Fares R., 2008, *MNRAS*, 388, 80
- Pizzolato N., Maggio A., Micela G., Sciortino S., Ventura P., 2003, *A&A*, 397, 147
- Rees D. E., Semel M. D., 1979, *A&A*, 74, 1
- Reid I. N., Hawley S. L., Gizis J. E., 1995, *AJ*, 110, 1838
- Reiners A., Basri G., 2006, *ApJ*, 644, 497
- Reiners A., Basri G., 2007, *ApJ*, 656, 1121
- Reiners A., Basri G., 2009, *A&A*, 496, 787
- Reiners A., Basri G., Browning M., 2009, *ApJ*, 692, 538
- Ribas I., 2006, *Ap&SS*, 304, 89
- Saar S. H., Linsky J. L., 1985, *ApJ*, 299, L47
- Schmitt J. H. M. M., Liefke C., 2004, *A&A*, 417, 651
- Semel M., Donati J.-F., Rees D. E., 1993, *A&A*, 278, 231
- Spiegel E. A., Zahn J.-P., 1992, *A&A*, 265, 106
- Wade G. A., Donati J.-F., Landstreet J. D., Shorlin S. L. S., 2000, *MNRAS*, 313, 851
- West A. A., Hawley S. L., Walkowicz L. M., Covey K. R., Silvestri N. M., Raymond S. N., Harris H. C., Munn J. A., McGehee P. M., Ivezić Ž., Brinkmann J., 2004, *AJ*, 128, 426

APPENDIX A: JOURNAL OF OBSERVATION

Table A1. Detailed journal of observations for GJ 51. Columns 1–7 list the UT date, the heliocentric Julian date, the UT time, the exposure time, the peak signal to noise ratio (per 2.6 km s^{-1} velocity bin) and the rms noise level (relative to the unpolarised continuum level and per 1.8 km s^{-1} velocity bin) in the average circular polarisation profile produced by Least-Squares Deconvolution (see Sec. 2.2). In column 7 we indicate the longitudinal field computed from Eq. 1. Column 8 lists the radial velocities (absolute accuracy 0.10 km s^{-1} , internal accuracy 0.03 km s^{-1}) associated to each exposure. The rotational cycle E from the ephemeris $\text{HJD} = 2453950 + 1.02 E$ is mentioned in column 9.

Date	HJD (2,450,000+)	UT (h:m:s)	t_{exp} (s)	S/N	σ_{LSD} ($10^{-4} I_c$)	B_ℓ (G)	RV (km s^{-1})	Cycle
2006								
Aug 05	3953.13879	15:15:58	4×450.0	121	12.6	-1617 ± 150	-5.24	3.077
Aug 07	3955.09204	14:08:29	4×550.0	132	9.3	-1126 ± 100	-5.37	4.992
Aug 08	3956.08931	14:04:27	4×650.0	165	7.7	-1105 ± 91	-5.43	5.970
Aug 09	3957.08253	13:54:37	4×500.0	139	9.0	-782 ± 94	-5.56	6.944
Aug 11	3959.09703	14:15:18	4×500.0	149	8.2	-673 ± 92	-5.80	8.919
Aug 12	3960.10164	14:21:51	4×500.0	128	10.1	-702 ± 103	-5.74	9.904
2007								
Sep 28	4371.97896	11:22:59	4×840.0	171	6.7	-1394 ± 96	-7.14	413.705
Sep 30	4374.02264	12:25:53	4×840.0	179	6.6	-1389 ± 94	-7.22	415.708
Oct 01	4374.94925	10:40:12	4×840.0	163	7.0	-2005 ± 111	-6.12	416.617
Oct 02	4375.82543	07:41:54	4×840.0	159	7.0	-1395 ± 101	-5.57	417.476
Oct 02	4375.94877	10:39:31	4×840.0	174	6.5	-2011 ± 108	-5.85	417.597
Oct 02	4376.05346	13:10:16	4×840.0	180	6.5	-1522 ± 97	-7.37	417.699
Oct 03	4376.82249	07:37:40	4×840.0	163	6.8	-1429 ± 104	-5.52	418.453
Oct 03	4376.94931	10:40:18	4×900.0	195	5.7	-2076 ± 108	-5.55	418.578
Oct 03	4377.05178	13:07:51	4×900.0	198	5.7	-1693 ± 95	-6.87	418.678
2008								
Oct 14	4753.82296	07:38:32	4×815.0	170	7.5	-1372 ± 90	-7.16	788.062
Oct 14	4753.86728	08:42:22	4×815.0	183	6.9	-1049 ± 79	-7.29	788.105
Oct 14	4753.96099	10:57:19	4×815.0	157	8.0	-619 ± 82	-6.63	788.197
Oct 14	4754.05403	13:11:17	4×815.0	159	7.6	-516 ± 81	-6.24	788.288
Oct 17	4756.85209	08:20:35	4×815.0	119	10.4	-1525 ± 105	-6.13	791.031
Oct 20	4759.77630	06:31:33	4×815.0	176	7.0	-1600 ± 84	-5.63	793.898
Oct 20	4759.85136	08:19:38	4×815.0	159	8.0	-1699 ± 95	-6.13	793.972
Oct 20	4759.94401	10:33:04	4×815.0	152	8.3	-1521 ± 93	-6.84	794.063
Oct 20	4760.03093	12:38:13	4×815.0	167	7.7	-1072 ± 85	-7.34	794.148

Table A2. Detailed journal of observations for GJ 1156. See Table A1 for more details. Data are phased according to the ephemeris $\text{HJD} = 2\,453\,950 + 0.491 E$.

Date	HJD (2,450,000+)	UT (h:m:s)	t_{exp} (s)	S/N	σ_{LSD} ($10^{-4}I_c$)	B_ℓ (G)	RV (km s^{-1})	Cycle
2007								
Mar 02	4162.05198	13:08:00	4×600.0	157	8.5	84 ± 67	5.86	431.878
Mar 03	4163.05912	13:18:14	4×420.0	120	11.0	177 ± 81	5.86	433.929
Mar 04	4164.04908	13:03:43	4×700.0	181	6.8	157 ± 59	5.83	435.945
Mar 05	4165.08932	14:01:37	4×600.0	165	7.7	-15 ± 65	5.80	438.064
Mar 06	4166.03032	12:36:37	4×500.0	143	9.3	91 ± 73	5.89	439.980
Mar 07	4167.00828	12:04:50	4×600.0	163	7.9	-2 ± 74	6.50	441.972
2008								
Jan 20	4485.98764	11:39:04	4×540.0	158	8.5	-264 ± 63	5.72	1091.625
Jan 20	4486.14332	15:23:14	4×540.0	156	8.4	148 ± 61	5.95	1091.942
Jan 21	4486.98190	11:30:41	4×540.0	127	10.4	-224 ± 74	5.61	1093.649
Jan 21	4487.14392	15:23:59	4×540.0	151	8.8	26 ± 65	5.95	1093.979
Jan 22	4488.09159	14:08:30	4×610.0	150	8.8	80 ± 65	5.83	1095.910
2009								
Jan 08	4840.01516	12:20:05	4×815.0	195	6.5	-187 ± 48	5.78	1812.658
Jan 08	4840.10476	14:29:06	4×815.0	187	6.5	55 ± 48	5.73	1812.841
Jan 08	4840.17094	16:04:23	4×815.0	166	8.8	168 ± 67	5.83	1812.975
Jan 09	4841.03123	12:43:05	4×815.0	167	7.7	-66 ± 55	5.10	1814.728
Jan 09	4841.09873	14:20:17	4×815.0	188	6.8	44 ± 50	5.77	1814.865
Jan 09	4841.16680	15:58:18	4×815.0	184	6.7	88 ± 49	5.97	1815.004
Jan 10	4842.02100	12:28:15	4×815.0	184	6.8	-105 ± 49	5.76	1816.743
Jan 10	4842.09687	14:17:29	4×815.0	183	6.9	81 ± 51	5.73	1816.898
Jan 10	4842.16403	15:54:11	4×815.0	187	6.7	135 ± 50	5.94	1817.035

Table A3. Detailed journal of observations for GJ 1245 B. See Table A1 for more details. Data are phased according to the ephemeris $\text{HJD} = 2\,453\,950 + 0.71 E$.

Date	HJD (2,450,000+)	UT (h:m:s)	t_{exp} (s)	S/N	σ_{LSD} ($10^{-4}I_c$)	B_ℓ (G)	RV (km s^{-1})	Cycle
2006								
Aug 05	3952.96705	11:05:26	4×630.0	166	8.6	-251 ± 33	5.29	4.179
Aug 08	3955.95886	10:53:38	4×700.0	191	7.1	-79 ± 26	5.40	8.393
Aug 09	3956.96600	11:03:55	4×600.0	175	7.7	186 ± 28	5.56	9.811
Aug 10	3957.95942	10:54:27	4×700.0	185	7.5	-179 ± 27	5.28	11.210
Aug 11	3958.96340	11:00:11	4×700.0	185	7.5	145 ± 27	5.52	12.625
Aug 12	3959.96518	11:02:45	4×700.0	158	8.8	-133 ± 29	5.48	14.035
2007								
Sep 30	4373.89061	09:17:56	4×840.0	197	6.8	-107 ± 27	5.30	597.029
Oct 01	4374.86550	08:41:51	4×840.0	199	6.6	148 ± 27	5.47	598.402
Oct 02	4375.72600	05:21:04	4×840.0	214	6.4	63 ± 26	5.51	599.614
Oct 02	4375.86847	08:46:14	4×840.0	182	7.4	-136 ± 29	5.26	599.815
Oct 03	4376.72595	05:21:05	4×900.0	226	5.7	-179 ± 25	5.27	601.022
Oct 03	4376.86630	08:43:13	4×900.0	218	6.0	108 ± 26	5.46	601.220
2008								
Aug 20	4698.75329	05:57:45	4×715.0	187	7.3	-44 ± 25	5.38	1054.582
Aug 20	4698.84202	08:05:31	4×715.0	191	7.3	-64 ± 26	5.34	1054.707
Aug 20	4698.99653	11:48:01	4×715.0	171	8.2	45 ± 28	5.52	1054.925
Aug 21	4699.75240	05:56:29	4×715.0	194	7.2	56 ± 25	5.52	1055.989
Aug 21	4699.87910	08:58:56	4×715.0	186	7.2	26 ± 26	5.53	1056.168
Aug 21	4699.99952	11:52:21	4×715.0	176	8.0	70 ± 27	5.60	1056.337
Aug 22	4700.74540	05:46:26	4×715.0	150	9.3	74 ± 32	5.44	1057.388
Aug 22	4700.87247	08:49:25	4×715.0	153	9.3	-138 ± 31	5.29	1057.567
Aug 22	4700.99137	11:40:38	4×715.0	151	9.6	-47 ± 32	5.45	1057.734
Aug 22	4701.02897	12:34:46	4×715.0	138	10.1	-41 ± 33	5.48	1057.787

Table A4. Detailed journal of observations for WX UMa. See Table A1 for more details. Data are phased according to the ephemeris $HJD = 2\,453\,850 + 0.78 E$.

Date	HJD (2,450,000+)	UT (h:m:s)	t_{exp} (s)	S/N	σ_{LSD} ($10^{-4}I_c$)	B_ℓ (G)	RV (km s^{-1})	Cycle
2006								
Jun 09	3895.77128	06:31:12	4×600.0	86	16.1	-1128 ± 213	70.39	0.476
Jun 09	3895.83862	08:08:10	4×600.0	67	19.8	-914 ± 207	70.60	0.562
Jun 10	3896.77760	06:40:22	4×600.0	137	11.9	-1816 ± 162	70.59	1.766
Jun 10	3896.84666	08:19:49	4×600.0	120	11.0	-2150 ± 198	70.78	1.855
Jun 11	3897.76780	06:26:19	4×600.0	142	9.6	-2053 ± 174	68.97	3.036
Jun 11	3897.83460	08:02:31	4×600.0	130	10.4	-1731 ± 119	70.21	3.121
Jun 12	3898.74596	05:54:56	4×600.0	122	11.2	-1147 ± 101	70.03	4.290
Jun 12	3898.81286	07:31:16	4×600.0	120	11.2	-1110 ± 103	70.43	4.375
2007								
Mar 02	4161.97902	11:26:01	4×700.0	143	8.8	-1825 ± 116	69.91	341.768
Mar 03	4162.99705	11:51:58	4×600.0	115	11.8	-1340 ± 124	70.04	343.073
Mar 04	4163.97675	11:22:44	4×700.0	154	8.4	-1581 ± 105	69.93	344.329
Mar 05	4165.01491	12:17:42	4×700.0	152	8.4	-2357 ± 124	69.90	345.660
Mar 07	4166.94370	10:35:10	4×560.0	137	10.0	-1265 ± 107	70.03	348.133
Mar 08	4168.03986	12:53:39	4×600.0	139	9.3	-2175 ± 125	69.92	349.538
2008								
Jan 19	4484.92606	10:10:43	4×560.0	63	21.4	-1416 ± 206	70.56	755.803
Jan 20	4486.11357	14:40:40	4×500.0	116	12.0	-1725 ± 115	70.01	757.325
Jan 21	4486.92292	10:06:06	4×540.0	123	11.2	-2135 ± 123	69.97	758.363
Jan 21	4487.11353	14:40:34	4×520.0	129	10.4	-1968 ± 114	70.05	758.607
2009								
Jan 11	4843.01564	12:20:02	4×715.0	116	11.9	-1147 ± 108	70.24	1214.892
Jan 11	4843.11846	14:48:06	4×715.0	113	12.5	-1151 ± 114	70.02	1215.024
Jan 12	4843.94502	10:38:18	4×715.0	132	10.0	-1670 ± 100	69.86	1216.083
Jan 12	4844.04478	13:01:57	4×715.0	113	12.2	-1707 ± 110	70.04	1216.211
Jan 12	4844.14627	15:28:05	4×715.0	133	10.0	-1772 ± 98	69.91	1216.341
Jan 13	4844.94269	10:34:54	4×715.0	133	10.0	-1638 ± 101	69.87	1217.362
Jan 13	4845.09115	14:08:40	4×715.0	146	9.0	-1864 ± 101	69.76	1217.553
Jan 13	4845.16697	15:57:51	4×715.0	153	8.4	-1735 ± 101	69.62	1217.650
Jan 14	4845.98095	11:29:57	4×715.0	145	9.2	-1274 ± 90	69.50	1218.694
Jan 14	4846.08129	13:54:25	4×715.0	163	8.0	-1366 ± 86	69.57	1218.822
Jan 14	4846.17078	16:03:17	4×715.0	158	8.4	-1130 ± 89	69.75	1218.937

Table A5. Detailed journal of observations for DX Cnc. See Table A1 for more details. Data are phased according to the ephemeris $\text{HJD} = 2\,453\,950 + 0.46 E$.

Date	HJD (2,450,000+)	UT (h:m:s)	t_{exp} (s)	S/N	σ_{LSD} ($10^{-4} I_c$)	B_ℓ (G)	RV (km s^{-1})	Cycle
2007								
Mar 02	4161.94084	10:30:16	4×700.0	165	8.8	145 ± 49	10.60	460.741
Mar 04	4163.93885	10:27:33	4×700.0	170	8.6	158 ± 47	10.52	465.084
Mar 05	4164.94533	10:36:57	4×700.0	179	8.3	-13 ± 46	10.65	467.272
Mar 06	4165.93747	10:25:43	4×560.0	119	12.3	209 ± 65	10.54	469.429
Mar 07	4166.91257	09:49:56	4×560.0	139	11.1	161 ± 55	10.46	471.549
2008								
Jan 18	4483.86547	08:40:11	4×520.0	116	12.7	81 ± 61	10.85	1160.577
Jan 19	4484.86323	08:36:58	4×560.0	141	10.6	34 ± 52	10.88	1162.746
Jan 19	4485.04885	13:04:15	4×570.0	90	16.7	86 ± 79	11.00	1163.150
Jan 20	4486.05051	13:06:39	4×600.0	161	9.4	11 ± 46	10.70	1165.327
Jan 21	4486.86360	08:37:30	4×560.0	138	10.9	135 ± 54	10.43	1167.095
Jan 21	4487.04831	13:03:28	4×700.0	160	9.8	131 ± 58	9.94	1167.496
Jan 22	4487.98223	11:28:19	4×610.0	152	9.5	166 ± 54	9.29	1169.527
2009								
Feb 13	4875.88471	09:08:28	4×800.0	122	12.3	86 ± 56	10.76	2012.793
Feb 14	4876.87737	08:57:56	4×800.0	137	11.6	149 ± 52	10.80	2014.951
Feb 14	4877.00055	11:55:19	4×800.0	106	14.8	-4 ± 65	10.68	2015.219
Feb 15	4877.75183	05:57:12	4×800.0	164	9.2	48 ± 43	10.66	2016.852
Feb 15	4877.87789	08:58:44	4×800.0	180	8.5	13 ± 40	10.49	2017.126
Feb 15	4878.01424	12:15:05	4×800.0	157	9.4	110 ± 44	10.58	2017.422
Feb 16	4878.76253	06:12:40	4×800.0	187	7.8	54 ± 37	10.61	2019.049
Feb 16	4878.88556	09:09:50	4×800.0	185	7.9	78 ± 36	10.78	2019.316
Feb 16	4879.00624	12:03:37	4×800.0	177	8.4	71 ± 38	10.71	2019.579

Table A6. Detailed journal of observations for GJ 3622. See Table A1 for more details. Data are phased according to the ephemeris $\text{HJD} = 2\,453\,950 + 1.5 E$.

Date	HJD (2,450,000+)	UT (h:m:s)	t_{exp} (s)	S/N	σ_{LSD} ($10^{-4} I_c$)	B_ℓ (G)	RV (km s^{-1})	Cycle
2008								
Mar 20	4545.85137	08:17:36	4×990.0	159	9.3	-50 ± 17	2.20	397.234
Mar 21	4546.94418	10:31:17	4×990.0	162	9.1	-2 ± 18	1.77	397.963
Mar 22	4548.00749	12:02:30	4×990.0	154	9.5	-20 ± 18	1.88	398.672
Mar 23	4548.92606	10:05:17	4×990.0	156	9.4	-72 ± 17	2.33	399.284
Mar 25	4550.82345	07:37:37	4×990.0	152	9.8	-60 ± 18	2.57	400.549
Mar 26	4551.82107	07:34:14	4×990.0	167	8.9	-56 ± 16	2.53	401.214
Mar 27	4552.91578	09:50:41	4×990.0	150	10.1	7 ± 18	2.46	401.944
Mar 28	4553.86120	08:32:08	4×990.0	128	11.1	-5 ± 20	2.41	402.574
2009								
Feb 13	4875.93524	10:18:39	4×900.0	101	15.0	-22 ± 26	2.35	617.290
Feb 15	4877.93049	10:11:42	4×900.0	134	11.0	-73 ± 20	2.44	618.620
Feb 16	4878.93305	10:15:21	4×900.0	151	10.0	-42 ± 18	2.32	619.289
Feb 16	4879.06535	13:25:51	4×900.0	135	11.3	-15 ± 19	2.37	619.377
Feb 17	4879.91581	09:50:29	4×900.0	162	9.3	13 ± 17	2.32	619.944
Feb 17	4880.05123	13:05:29	4×900.0	151	10.0	-18 ± 18	2.42	620.034

Table A7. Detailed journal of observations for GJ 1154 A. See Table A1 for more details. The rotational cycle is not indicated since no rotation period could be derived for this star.

Date	HJD (2,450,000+)	UT (h:m:s)	t_{exp} (s)	S/N	σ_{LSD} ($10^{-4}I_c$)	B_ℓ (G)	RV (km s^{-1})
2007							
Mar 02	4162.01888	12:19:34	4×600.0	150	7.9	-825 ± 63	-12.76
Mar 03	4163.03213	12:38:35	4×500.0	118	10.5	-672 ± 69	-12.79
Mar 04	4164.01521	12:14:11	4×600.0	167	7.0	-718 ± 55	-12.77
Mar 05	4165.05486	13:11:23	4×600.0	147	7.2	-612 ± 55	-13.07
Mar 06	4166.00262	11:55:57	4×500.0	152	8.1	-660 ± 59	-12.82
Mar 07	4166.97810	11:20:36	4×500.0	140	8.6	-800 ± 62	-12.78
2008							
Jan 19	4485.01555	12:18:53	4×540.0	86	15.9	-576 ± 85	-12.81
Jan 20	4486.01710	12:20:59	4×500.0	147	8.2	-776 ± 57	-12.89
Jan 21	4487.01179	12:13:12	4×540.0	130	9.3	-721 ± 61	-12.76
Jan 22	4488.01494	12:17:37	4×610.0	154	8.3	-727 ± 61	-13.22

Table A8. Detailed journal of observations for GJ 1224. See Table A1 for more details. The rotational cycle is not indicated since no rotation period could be derived for this star.

Date	HJD (2,450,000+)	UT (h:m:s)	t_{exp} (s)	S/N	σ_{LSD} ($10^{-4}I_c$)	B_ℓ (G)	RV (km s^{-1})
2008							
Jun 25	4643.02829	12:33:21	4×800.0	176	6.2	-535 ± 36	-32.75
Jun 28	4645.88511	09:07:15	4×800.0	51	19.7	-546 ± 95	-32.69
Jun 28	4645.92645	10:06:46	4×800.0	86	14.1	-631 ± 67	-32.62
Jun 29	4646.94450	10:32:47	4×800.0	147	7.9	-550 ± 42	-32.67
Jul 02	4649.94447	10:32:50	4×800.0	155	7.3	-632 ± 41	-32.72
Jul 03	4650.91640	09:52:27	4×800.0	171	6.6	-550 ± 37	-32.69
Jul 04	4651.85383	08:22:23	4×800.0	171	6.3	-556 ± 37	-32.64
Jul 05	4652.86038	08:31:51	4×800.0	176	6.1	-617 ± 37	-32.69
Jul 06	4653.83070	07:49:09	4×800.0	185	5.8	-545 ± 34	-32.64
Jul 07	4654.89004	09:14:39	4×800.0	166	6.6	-573 ± 38	-32.65
Jul 08	4655.84785	08:13:57	4×800.0	172	6.4	-523 ± 37	-32.63
Jul 09	4656.96336	11:00:20	4×800.0	172	6.4	-500 ± 40	-32.72

Table A9. Detailed journal of observations for CN Leo. See Table A1 for more details. The rotational cycle is not indicated since no rotation period could be derived for this star.

Date	HJD (2,450,000+)	UT (h:m:s)	t_{exp} (s)	S/N	σ_{LSD} ($10^{-4}I_c$)	B_ℓ (G)	RV (km s^{-1})
2008							
Mar 21	4546.99345	11:43:06	4×800.0	179	5.6	-651 ± 45	19.66
Mar 22	4547.91616	09:51:50	4×800.0	172	6.7	-635 ± 48	19.68
Mar 22	4547.95840	10:52:40	4×800.0	186	6.1	-708 ± 46	19.63
Mar 23	4548.87485	08:52:23	4×800.0	245	4.5	-772 ± 45	19.55

Table A10. Detailed journal of observations for VB 8. See Table A1 for more details. The rotational cycle is not indicated since no rotation period could be derived for this star.

Date	HJD (2,450,000+)	UT (h:m:s)	t_{exp} (s)	S/N	σ_{LSD} ($10^{-4}I_c$)	B_ℓ (G)	RV (km s^{-1})
2009							
May 03	4954.89250	09:18:10	4×1154.0	104	16.5	24 ± 29	15.41
May 03	4954.99885	11:51:19	4×1154.0	107	15.8	-15 ± 28	15.24
May 03	4955.10357	14:22:06	4×1154.0	107	15.7	-52 ± 28	15.39
May 04	4955.90408	09:34:47	4×1154.0	83	20.0	113 ± 36	15.63
May 04	4956.00991	12:07:11	4×1154.0	94	17.9	49 ± 32	15.41
May 04	4956.11013	14:31:29	4×1154.0	98	17.0	-25 ± 30	15.31
May 05	4956.90261	09:32:37	4×1154.0	99	16.9	77 ± 30	15.31
May 05	4957.00469	11:59:36	4×1154.0	102	16.2	87 ± 29	15.32
May 05	4957.11128	14:33:05	4×1154.0	103	16.3	5 ± 29	15.51

Table A11. Detailed journal of observations for VB 10. See Table A1 for more details. The rotational cycle is given for the most probable period according to the ephemeris $\text{HJD} = 2\,455\,000 + 0.69 E$.

Date	HJD (2,450,000+)	UT (h:m:s)	t_{exp} (s)	S/N	σ_{LSD} ($10^{-4}I_c$)	B_ℓ (G)	RV (km s^{-1})	Cycle
2009								
Jul 01	5013.96290	10:58:52	4×1154.0	68	25.7	94 ± 65	36.16	20.236
Jul 01	5014.01972	12:20:41	4×1154.0	77	23.0	92 ± 57	36.25	20.318
Jul 01	5014.07652	13:42:29	4×1154.0	76	23.0	145 ± 57	36.03	20.401
Jul 02	5014.95765	10:51:17	4×1154.0	71	24.2	16 ± 59	36.25	21.678
Jul 02	5015.01489	12:13:42	4×1154.0	74	23.4	68 ± 57	36.37	21.761
Jul 02	5015.10842	14:28:23	4×1154.0	80	22.5	93 ± 58	36.13	21.896
Jul 03	5015.94279	10:29:52	4×1154.0	74	23.1	-69 ± 59	36.27	23.105
Jul 03	5016.04819	13:01:38	4×1154.0	75	23.6	-4 ± 56	36.51	23.258
Jul 03	5016.10641	14:25:28	4×1154.0	74	23.5	92 ± 61	36.13	23.343